


Phenomenological model of gravitational self-force enhanced tides in inspiralling binary neutron stars

Natalie Williams ^{1,*} Patricia Schmidt ^{1,†} and Geraint Pratten ^{1,‡}

¹*School of Physics and Astronomy and Institute for Gravitational Wave Astronomy, University of Birmingham, Edgbaston, Birmingham, B15 2TT, United Kingdom*

Gravitational waves from inspiralling binary neutron stars provide unique access to ultra-dense nuclear matter and offer the ability to constrain the currently unknown neutron star equation-of-state through tidal measurements. This, however, requires the availability of accurate and efficient tidal waveform models. In this paper we present PHENOMGSF, a new phenomenological tidal phase model for the inspiral of neutron stars in the frequency-domain, which captures the gravitational self-force informed tidal contributions of the time-domain effective-one-body model TEOBRESUMS. PHENOMGSF is highly faithful and computationally efficient, and by choosing a modular approach, it can be used in conjunction with *any* frequency-domain binary black hole waveform model to generate the complete phase for a binary neutron star inspiral. PHENOMGSF is valid for neutron star binaries with unequal masses and mass ratios between 1 and 3, and dimensionless tidal deformabilities up to 5000. Furthermore, PHENOMGSF does not assume universal relations or parameterised equations-of-state, hence allowing for exotic matter analyses and beyond standard model physics investigations. We demonstrate the efficacy and accuracy of our model through comparisons against TEOBRESUMS, numerical relativity waveforms and full Bayesian inference, including a reanalysis of the binary neutron star observation GW170817.

I. INTRODUCTION

Detections of gravitational waves (GWs) from binary neutron stars (BNS) hold the potential to probe nuclear matter at densities which cannot easily be achieved under laboratory conditions, and shed light on the currently unknown neutron star equation-of-state (EOS) [1, 2]. The observation of the inspiralling BNS GW170817 [3, 4] provided the first constraints on the EOS obtained from GWs. Complementary EOS constraints for nuclear matter can be obtained from X-ray observations of pulsars [5, 6] or the measurement of the thickness of the neutron skin in laboratory experiments [7, 8]. Notable differences in inferred constraints on the neutron star radius between different astrophysical and laboratory-based measurements [9], however, highlight the crucial role of more observations, e.g. from GWs and NICER to resolve the tension.

Matter leaves characteristic imprints on the GW signal, making the signal distinct from that of a binary black hole (BBH). The most prominent GW signature arises from the excitation of a neutron star’s fundamental oscillation modes or f -modes, which, at leading order, is characterised by the quadrupolar tidal deformability λ_2 [1]. Its measurement in GW observations allows us to constrain the EOS [10]. However, in order to do so, waveform models that accurately capture the relevant physics are needed. Current state-of-the-art tidal waveform models are obtained either within post-Newtonian (PN) theory [1, 11–18], the effective-one-body (EOB)

framework [12, 19–27], or by utilising a phenomenological approach [28–32]. One particular advantage of phenomenological waveform models is their computational efficiency, which is highly desirable when performing Bayesian inference which often requires $\sim 10^6$ – 10^9 model evaluations to accurately sample the posterior distributions. The computational efficiency of phenomenological models is achieved by directly describing the waveform as piecewise closed-form expressions in the frequency domain by fitting ansatzes for the amplitude and phase to hybrid waveforms, which combine state-of-the-art analytical knowledge with numerical relativity (NR) waveforms. This approach has been successfully applied to obtain fast waveform models for binary black holes [33–39], neutron star – black hole binaries [40, 41] and BNSs [29, 30]. Alternative approaches to decreasing the waveform generation cost include the stationary phase approximation (SPA) [42] and reduced-order modelling [43]. Parameter estimation itself can also be sped up by techniques such as relative binning [44–48], multi-banding [49, 50] and reduced-order quadratures [51–54].

Current BNS waveform models do not only differ in their computational speed but also in their physics content. In particular, the phenomenological models of the NRTIDAL series [28–30] are calibrated to a limited range of BNS simulations. While this allows for the incorporation of non-perturbative information, it also comes with some caveats: firstly, the NR data are themselves limited in their physics content due to the complexity of matter simulations. Secondly, different tidal effects that arise in the strong-field regime such as higher-order multipoles or other oscillation modes including pressure (p -) and gravity (g -) modes, are difficult to separate in NR simulations and hence when modelled phenomenologically are entangled in the parameterisation. Thirdly, NR simulations make specific assumptions on the nuclear EOS

* nxw049@student.bham.ac.uk

† P.Schmidt@bham.ac.uk

‡ G.Pratten@bham.ac.uk

such a hadronic composition. Finally, to reduce the dimensionality of the parameter space, tidal models also often invoke quasi-EOS independent universal relations (URs) [55] between different tidal parameters. While this dimensional reduction may be desirable, any such assumptions will limit the applicability of the model and exclude them from being used for exploring e.g. the possibility of the presence of exotic matter such as hyperons or deconfined quarks or boson stars [56].

In this work we present PHENOMGSF, a new phenomenological tidal phase model in the frequency-domain based on the tidal EOB model TEOBRESUMS [24], which can readily be added to *any* BBH baseline to provide a complete BNS model. We restrict our model to the dominant tidal effects associated with the quadrupolar gravitoelectric static Love number k_2 including tidal contributions informed by gravitational self-force (GSF), and only model the phase of the $\ell = |m| = 2$ mode. PHENOMGSF is calibrated to both equal and unequal mass systems and freely fits the component tidal deformabilities without assuming URs, hadronic matter or specific parameterisations of the EOS.

The paper is organised as follows: Section II details some preliminaries, the used conventions and parameterisations. In Sec. III we specify the input waveforms used to build the model, the parameter space of the model and detail the construction of TEOBRESUMS-NR hybrid waveforms. Then, in Sec. IV we detail the hierarchical phenomenological fitting procedure and give details of the model construction. In Sec. V we validate our model against the input waveforms, a set of independent waveforms as well as a selection of NR-hybrid waveforms. We then perform Bayesian inference with PHENOMGSF on model injections, a hybrid waveform and reanalyse the data of GW170817. We then conclude with a discussion in Sec. VI. The complete PHENOMGSF fit can be found in App. A, while the full parameter estimation results for GW170817 are shown in App. B. Throughout the paper we use geometric units by setting $G = c = 1$.

II. PRELIMINARIES

A. Tidal Parameterisations

As opposed to BBH systems, the presence of matter in a BNS system induces an additional quadrupole moment and hence accelerates the inspiral. Physically, this results in a multipolar deformation of each neutron star, which, at leading-order, is characterised by the static quadrupolar $\ell = 2$ (dimensionless) tidal deformability $\Lambda_{i,2} = \lambda_{i,2}/m_i^5$ of the i -th star with mass m_i . The tidal deformability strongly depends on the internal structure of the neutron star and hence is connected to the EOS. Its measurement can therefore be used to map macroscopic properties to a constraint on the microscopic EOS. As we only consider the $\ell = 2$ multipole, we drop the multipolar index henceforth for convenience. We also define the

total mass $M = m_1 + m_2$, mass ratio $q = m_1/m_2 \geq 1$ and symmetric mass ratio $\eta = q/(1+q)^2$.

In PN theory, the leading-order tidal effect in the GW phase occurs at 5PN [1] and is governed by the parameter [57]

$$\tilde{\Lambda} = \frac{8}{13} \left[(1 + 7\eta - 31\eta^2)(\Lambda_1 + \Lambda_2) + \sqrt{1 - 4\eta}(1 + 9\eta - 11\eta^2)(\Lambda_1 - \Lambda_2) \right]. \quad (2.1)$$

The coefficient of the next-to-leading correction is given by [2, 57]

$$\delta\tilde{\Lambda} = \frac{1}{2} \left[\sqrt{1 - 4\eta} \left(1 - \frac{13272}{1319}\eta - \frac{8944}{1319}\eta^2 \right) (\Lambda_1 + \Lambda_2) + \left(1 - \frac{15910}{1319}\eta - \frac{32850}{1319}\eta^2 + \frac{3380}{1319}\eta^3 \right) (\Lambda_1 - \Lambda_2) \right]. \quad (2.2)$$

While we will be sampling the binary parameter space in $\{q, \Lambda_1, \Lambda_2\}$ to build our training dataset, we will then transform to $\{\eta, \tilde{\Lambda}, \delta\tilde{\Lambda}\}$ to construct the PHENOMGSF model.

B. Waveform Conventions

PHENOMGSF models the phase of the $\ell = |m| = 2$ spin-weighted spherical harmonic modes of the GW signal of nonspinning neutron star inspirals. The complex GW strain as a function of GW frequency f is given by

$$\tilde{h} \equiv \tilde{h}_+(f, \vec{\theta}, \vartheta, \varphi) - i\tilde{h}_\times(f, \vec{\theta}, \vartheta, \varphi) \quad (2.3)$$

$$= \sum_{m=\{-2,2\}} \tilde{h}_{2m}(f, \vec{\theta})^{-2} Y_{2m}(\vartheta, \varphi), \quad (2.4)$$

where $\vec{\theta}$ denotes the intrinsic source parameters, (ϑ, φ) the orientation of the binary with respect to an observer, and $^{-2}Y_{2m}$ the spherical harmonic of spin weight $s = -2$ given by

$$^{-2}Y_{2\pm 2}(\vartheta, \varphi) = \sqrt{\frac{5}{64\pi}} (1 \pm \cos\vartheta)^2 e^{\pm 2i\varphi}. \quad (2.5)$$

We utilise the orbital plane reflection symmetry of aligned spin systems to map between the $(m = 2)$ -mode and $(m = -2)$ -mode via

$$\tilde{h}_{22}(f, \vec{\theta}) = \tilde{h}_{2,-2}^*(-f, \vec{\theta}), \quad (2.6)$$

where $*$ denotes complex conjugation.

Each mode can be further decomposed into an amplitude $A_{\ell m}(f, \vec{\theta})$ and a phase $\psi_{\ell m}(f, \vec{\theta})$. The presence of tides predominantly affects the phase, although there are

small amplitude corrections [58], which we do not take into account here, yielding

$$\tilde{h}_{22}(f, \vec{\theta}) = A_{22}^{\text{BBH}}(f, \vec{\theta}) e^{-i\psi_{22}(f, \vec{\theta})}, \quad (2.7)$$

where $\psi_{\ell m}$ denotes the complete Fourier phase given by the point particle phase plus the tidal phase

$$\psi_{\ell m} = \psi_{\ell m}^{\text{BBH}} + \psi_{\ell m}^{\text{PHENOMGSF}} + \psi_{\ell m}^{\text{SS}}, \quad (2.8)$$

where $\psi_{\ell m}^{\text{SS}}$ denotes the tidal self-spin PN corrections [59, 60] described in more detail in Sec. IV D.

III. INPUT WAVEFORMS

A. TEOBResumS Waveforms

The EOB framework provides a map from the general relativistic two-body problem to the motion of a test particle in a deformed effective spacetime. The EOB formalism allows one to calculate the full orbital dynamics and the complete waveform through merger. The EOB Hamiltonian describes the conservative dynamics with dissipative effects entering through the radiation reaction force in the equations of motion. Here we provide a brief overview of how tidal effects enter the TEOBRESUMS [24], with a particular focus on the GSF-resummed tidal potentials in the Hamiltonian introduced in [61] and extended in [25, 31]. We emphasise that no NR information is included in the tidal sector. Tidal contributions also enter the radiation reaction force within the waveform multipoles as PN corrections to the amplitude (see [27] for more details). The EOB tidal model outlined here sets the baseline for the tidal content included in the PHENOMGSF calibration dataset.

Tidal forces enter the Hamiltonian through a modification of the EOB radial potential

$$A(u) = A_0(u) + A_T(u), \quad (3.1)$$

where $u = 1/r$ is the Newtonian potential, $A_0(u)$ denotes the point-particle potential, and $A_T(u)$ encodes the tidal interactions [62]

$$A_T(u) = \sum_{\ell} \left[A_A^{(\ell+)\text{LO}}(u) \hat{A}^{(\ell+)}(u) + A^{(\ell-)\text{LO}}(u) \hat{A}^{(\ell-)}(u) \right] + (A \leftrightarrow B), \quad (3.2)$$

where A, B label the stars, $(+)$ denotes the gravitoelectric sector, $(-)$ the gravitomagnetic sector, and \hat{A} denotes terms beyond leading-order (LO).

The gravitoelectric tidal coefficients broadly relate to mass multipole moments induced in a star by an external gravitoelectric tidal field and the gravitomagnetic tidal coefficients to the current multipoles moments induced in a star by an external gravitomagnetic field [62]. The gravitomagnetic tides are therefore typically associated

to frame-dragging effects which in turn excite inertial modes in the NS [63–65], including those that are associated to the Coriolis effect. As we predominantly focus on non-spinning binaries, we choose not to implement the gravitomagnetic terms at this time. The following therefore pertains only to the gravitoelectric tides. Likewise, we restrict ourselves to the dominant $\ell = 2$ quadrupole and disregard all higher multipole moments unless otherwise stated.

Under the above restrictions, the Newtonian tidal potential can be written as

$$A^{\text{LO}}(u) = -\kappa_A u^6, \quad (3.3)$$

where κ_A denotes the electric tidal coupling constant, which can be expressed in terms of the dimensionless tidal love number $k_A^{(\ell)}$ as

$$\kappa_A = 2k_A^{(2)} \frac{X_B}{X_A} \left(\frac{X_A}{C_A} \right)^5, \quad (3.4)$$

$$= 3X_B X_A^4 \Lambda_A, \quad (3.5)$$

where $C_A = m_A/R_A$ denotes the compactness parameter, and the dimensionless tidal deformability is related to the Love number via

$$\Lambda_A = \frac{2}{3} k_A^{(2)} C_A^{-5}. \quad (3.6)$$

The EOB radial potential subsequently simplifies to

$$A_T = -[\kappa_A u^6 \hat{A}_A(u) + \kappa_B u^6 \hat{A}_B(u)]. \quad (3.7)$$

Following [25, 61], the terms beyond LO admit a series expansion in terms of the expansion parameter $X_A = m_A/M \ll 1$, informed by results at first-order GSF

$$\hat{A}_A(u) = \hat{A}^{0\text{GSF}} + X_A \hat{A}^{1\text{GSF}} + X_A^2 \hat{A}^{2\text{GSF}}. \quad (3.8)$$

The 0GSF potential is given by [61]

$$\hat{A}^{0\text{GSF}}(u) = 1 + \frac{3u^2}{1 - r_{\text{LR}}u}, \quad (3.9)$$

where r_{LR} denotes the EOB light-ring (LR).

The 1GSF potential is expressed in terms of the LR singularity together with a fit against strong-field GSF information [25]

$$\hat{A}^{1\text{GSF}} = \frac{5u}{2(1-3u)^{7/2}} (1 - a_1 u)(1 - a_2 u) \frac{1 + n_1 u}{1 + d_2 u^2} \quad (3.10)$$

with coefficients

$$\begin{aligned} a_1 &= 8.53352 & a_2 &= 3.04309 \\ n_1 &= 0.84006 & d_2 &= 17.7324. \end{aligned} \quad (3.11)$$

In contrast, the 2GSF potential only incorporates partial knowledge of the second-order GSF result [20]

$$X_A^2 \hat{A}_A^{2\text{GSF}}(u) = \frac{337}{28} X_A^2 u^2 (1 + \mathcal{O}(u)), \quad (3.12)$$

such that near the LR, the quadrupolar electric tidal potential must blow up as [61]

$$\frac{c_2 X_A^2}{(1 - r_{\text{LR}} u)^p}, \quad p \geq 4. \quad (3.13)$$

The 2GSF tidal potentials can therefore be written as

$$\hat{A}^{2\text{GSF}} = \frac{337}{28} \frac{u^2}{(1 - r_{\text{LR}} u)^p}, \quad (3.14)$$

where the value of p depends on as-of-yet-unknown 2GSF information. It was argued in [61] that $p \geq 4$ together with a further argument that $p \leq 6$. Following [25, 31], the unknown exponent is taken to be $p = 4$, though both coefficients may generically have mass ratio and EOS dependence.

We choose to not include dynamical tidal effects within PHENOMGSF, which would further increase the dimensionality of the parameter space, corresponding to each stars fundamental mode frequency ω_2 , unless we use universal relations to relate the values of ω_2 to Λ_2 . We note that due to the modularity of our model, it is in principle straight forward to incorporate the PN dynamical tides using the FMTIDAL model [16].

As TEOBRESUMS is natively defined in the time-domain, we need to transform the model to frequency-domain in order to calibrate PHENOMGSF. We use the numerical SPA implemented in TEOBRESUMS [66]

$$\frac{d^2 \psi(f)}{d\omega} = \frac{1}{\omega} \frac{d\psi(t)}{d\omega},$$

where $\omega = 2\pi f = \dot{\psi}(t)$. We use the SPA over a full Fourier transform due to small dephasing that was arising from spectral leakage and tapering in the binary black hole limit. We independently verified that the SPA agrees with the Fourier transform on a sub-radian scale over the parameter space under consideration.

B. Parameter Space

PHENOMGSF is calibrated across the parameter space $q \in [1, 3]$ and $\Lambda_{1,2} \in [0, 5000]$ using 8446 TEOBRESUMS waveforms. The total mass M scales out of the tidal phase when we consider the phase as a function of geometric frequency Mf . This allows us to reduce the problem to a 3-dimensional parameter space governed by a single mass parameter, taken to be either q or η .

For sampling the mass ratio, we choose a log-uniform spacing in order to have higher resolution near the equal-mass limit $q = 1$. Due to the hierarchical fitting process employed later on and explained in Sec. IV, a subset of 446 of these waveforms was specifically generated such that $\delta\tilde{\Lambda} = 0$. Within this subset, $\tilde{\Lambda}$ is uniformly sampled between the limits defined by a given q for $\Lambda_{1,2} \in [0, 5000]$. An additional layer of log-uniform spaced waveforms with $\tilde{\Lambda} \in [0, 200]$ is also added in order to accurately capture the approach to the black hole

limit, i.e. $\tilde{\Lambda} = 0$. The remaining 8000 waveforms are sampled uniformly directly in $\Lambda_{1,2}$, including another log-uniform layer inserted between $\Lambda_{1,2} = 0$ and the first uniformly chosen point. A visualisation of the calibration region is shown in Fig. 1.

An important point to note is that we do not assume hadronic physics, i.e. we do not enforce for $q \neq 1$, $\Lambda_2 > \Lambda_1$, and for $q = 1$, $\Lambda_2 = \Lambda_1$ when sampling the training space. This is done deliberately to ensure that the model is well-behaved without imposing such limiting assumptions and that no pathologies occur.

This is a particular strength of PHENOMGSF as it allows for more flexibility and separates it from models that are informed by NR data that assume a hadronic EOS. Consequently, this also allows the consideration of objects such as boson stars and quark stars and other exotic models which are not comprised of hadronic matter.

When generating the TEOBRESUMS waveforms, we choose a sampling rate of 16384 Hz and a starting frequency of 10 Hz below the equivalent of $0.0005Mf$ in Hz for a given total mass M to allow for a buffer between the start of the waveform and the fitting regime. We stop the EOB evolution at an orbital separation of $r = 4M$. We also explicitly turn off gravitomagnetic tides, dynamical tides, the use of universal relations, and set the octupolar and hexadecapolar tidal deformabilities to 10^{-8} , the lowest possible value we found.

C. TEOBResumS-NR Hybrids

For the model validation of PHENOMGSF we perform comparisons against a set of six TEOBRESUMS-NR hybrid waveforms. The NR waveforms are taken from the CoRe database [67–69] and were produced with the BAM code (see Refs. in [68] for details), which we hybridise with TEOBRESUMS waveforms using identical settings to those used for the calibration of PHENOMGSF and generated from 30 Hz. Details of the six aligned-spin NR waveforms used in this paper are given in Tab. I. The choice of these simulations is motivated by simulation length requirements and minimal residual eccentricity.

Our $(\ell, m) = (2, 2)$ hybrids are generated as follows: We take the Newman-Penrose scalar $\psi_{4,22}$ at the largest fixed extraction radius available r_0 the simulation and extrapolate it to infinity via [72, 73]

$$\begin{aligned} \psi_{4,22}^\infty(t, r_0) &= \left(1 - \frac{2M_{\text{ADM}}}{r_A}\right) \\ &\times \left[\psi_{4,22}^{r_0}(t, r_0) - \frac{2}{r_A} \int_0^t \psi_{4,22}^{r_0}(t', r_0) dt'\right], \end{aligned} \quad (3.15)$$

where $r_A = r_0[1 + M_{\text{ADM}}/(2r_0)]^2$ and M_{ADM} is the ADM mass of the system [74] obtained from the CoRE metadata.

The Newman-Penrose scalar is related to gravitational-

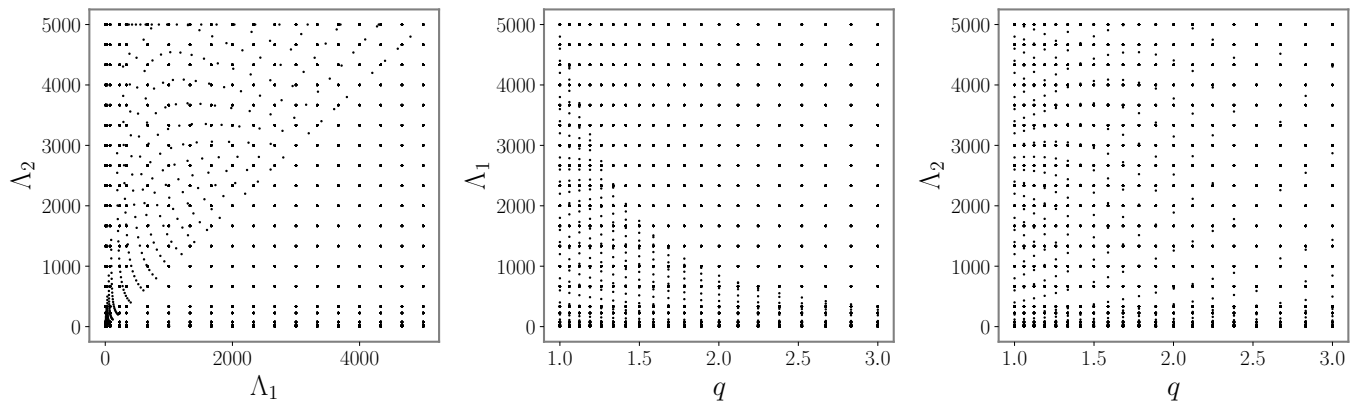


FIG. 1. Visualisation of the parameter space covered by the TEOBRESUMS waveforms used in the calibration of PHENOMGSF.

CoRE ID	EOS	$M_{\text{ADM}} [M_{\odot}]$	q	Λ_1	Λ_2	χ_{1z}	χ_{2z}	e	f_{NR} [Hz]	Ref.
BAM 0001	2B	3.05	1.0	126.7	126.7	0.0	0.0	7.0×10^{-3}	454.5	[31]
BAM 0120	SLy	3.05	1.0	346.1	346.1	0.0	0.0	1.5×10^{-2}	424.4	[70]
BAM 0127	SLy	3.07	1.5	93.1	1367.9	0.0	0.0	8.0×10^{-3}	426.3	[70]
BAM 0124	SLy	2.76	1.5	191.0	2313.7	0.0	0.0	1.2×10^{-2}	407.8	[70]
BAM 0104	SLy	2.99	1.0	388.2	388.2	0.19	0.19	7.4×10^{-4}	453.1	[28]
BAM 0066	MS1b	2.94	1.0	1531.5	1531.5	0.18	0.18	1.9×10^{-3}	427.2	[28]
BAM 0095	SLy	2.7	1.0	390.1	390.1	0.0	0.0	4.0×10^{-4}	453.3	[28]

TABLE I. Summary of the parameters of the aligned-spin NR waveforms from the CoRe database used to create the TEOBRESUMS-NR hybrids. The columns denote the CoRE ID number, the EOS [71] used for the simulations, the ADM mass M_{ADM} , mass ratio q , tidal deformabilities Λ_1, Λ_2 , component spins χ_1, χ_2 , the residual eccentricity e , the NR starting frequency f_{NR} , and relevant references. All quantities are taken from the CoRE metadata.

wave strain $h_{22}(t)$ via

$$\psi_{4,22}(t) = \frac{d^2 h_{22}(t)}{dt^2}. \quad (3.16)$$

We implement this double time-integration via the fixed frequency integration (FFI), where the waveform is windowed such that it smoothly tapers to zero below $t = 200M$ to remove any residual “junk radiation” at the start of the NR waveform due to imperfect initial data. We also taper to zero at an arbitrary time just after merger for each waveform to avoid edge effects in the FFI. The waveform is then zero-padded to reduce any spectral leakage. We implement the FFI following Ref. [75] choosing the NR starting frequency f_{NR} given in Tab. I as the fixed-frequency to perform the integration.

The NR waveforms are then hybridised with TEOBRESUMS waveforms, where all settings are the same as those detailed in Sec. III for the TEOBRESUMS generation with the exception of using the time-domain rather than the SPA implementation. The TEOBRESUMS waveforms are initialised with the same intrinsic parameters as the NR simulations. We note here that we

used the non-eccentric version of TEOBRESUMS, however, the NR waveforms have non-negligible eccentricity as shown in Tab. I, which constitutes a source of error in the hybridisation procedure.

For the hybridisation between the NR and TEOBRESUMS waveforms, we first ensure that the amplitudes of both waveforms peak at $t = 0$, and then choose a Planck window $\sigma(t)$ [76] across a time interval $[t_1, t_2]$ to smoothly join the two waveforms such that

$$\sigma(t) = \begin{cases} 0 & \text{if } t < t_1, \\ \frac{1}{1+e^z}, z = \frac{t}{t_1} - \frac{t_2}{t_1} & \text{if } t_1 \leq t \leq t_2, \\ 1 & \text{if } t > t_2, \end{cases} \quad (3.17)$$

where we find that $t_1 = 1200M$ (with the exception of BAM 0095, where $t_1 = 1000M$) after the start of the NR waveform and a window length of $1000M$ are sufficient. Across this window a time domain alignment is performed by minimising

$$\min \left[\int_{t_1}^{t_2} \left| \psi^{\text{TEOB}}(t) - \psi^{\text{NR}}(t + t_0) - 2\psi_0 \right|^2 dt \right], \quad (3.18)$$

and a visual inspection to check for the continuity of amplitude, phase and phase derivative is done as shown in Fig. 2.

IV. TIDAL PHASE MODEL

A. Phenomenological Modelling

A key motivation for building phenomenological (Phenom) waveform models is that they can yield closed-form frequency-domain expressions, making them extremely computationally efficient for GW data analysis whilst retaining a high level of accuracy. As a result, Phenom models have become a very popular choice in many aspects of gravitational-wave data analysis, including matched-filter searches, e.g. [77–82], and Bayesian inference, e.g. [83–91]. We note that an alternative phenomenological model of TEOBRESUMS using a different approach was developed in Ref. [27].

In PHENOMGSF, we follow the framework previously described for the BBH waveform model IMRPHENOMXAS [36]. We will first briefly outline the main elements in the construction of a phenomenological phase model before presenting the detailed fits in the remainder of this section.

We recall that the goal is to build a closed-form expression of the tidal phase of binary neutron stars in the frequency domain. The first step is to choose an appropriate mathematical ansatz for the tidal phase for each section of the different stages of the binary evolution. As we are only considering the inspiral phase here with a known PN expansion, a natural choice is a parameterised continuation of the finite-order PN series, schematically given by

$$\psi_T(\vec{\theta}, Mf) = \psi_T^{\text{PN}}(\vec{\theta}, Mf) + \sum_i a_i(\vec{\theta})(Mf)^i, \quad (4.1)$$

where $\vec{\theta}$ denotes the model parameters and Mf is the dimensionless GW frequency.

Note that the powers of the frequency are for illustrative purposes only. In the latest generation of phenomenological models, the phenomenological coefficients $a_i(\vec{\theta})$ are not directly calibrated due to numerical instabilities and poor numerical conditioning [36]. Instead, the phenomenological coefficients are reconstructed by solving a linear system of equations expressed in terms of a finite number of collocation points that are placed at prescribed frequency nodes, $\{Mf_j\}$.

In order for this to be a deterministic system, the number of constraints, e.g. boundaries, *and* collocation points must equal the total number of free parameters. At each collocation point, a fit is constructed such that

$$\lambda_j(\vec{\theta}) \equiv \psi_T(\vec{\theta}, Mf_j). \quad (4.2)$$

The resulting linear system of equations can then be solved for the phenomenological coefficients using standard matrix methods, e.g. via an LU decomposition.

B. Tidal Residual Fit

For the PN baseline, we use TAYLORF2 with quadrupolar adiabatic tidal contributions up to 7.5PN [12, 18, 20]. We add five pseudo-PN coefficients a^i that are calibrated to the TEOBRESUMS dataset

$$\psi_{\ell m}^{\text{PHENOMGSF}} = \psi_T^{7.5\text{PN}} + \sum_{i=1}^5 a^i(\eta, \tilde{\Lambda}, \delta\tilde{\Lambda})(Mf)^{(10+i)/3}. \quad (4.3)$$

Instead of directly fitting the phase, we fit the residual between TEOBRESUMS and TaylorF2,

$$r \equiv \psi_T^{\text{TEOB}} - \psi_T^{7.5\text{PN}} - 2\pi Mf t_0 + \phi_0, \quad (4.4)$$

where $\{t_0, \phi_0\}$ are two gauge degrees of freedom corresponding to an overall time and phase shift and are determined by minimising the residuals over a frequency interval

$$\min \left[\int_{0.0005M}^{0.001M} |r|^2 dMf \right]. \quad (4.5)$$

A choice that must be made is the PN baseline for the phenomenological model. It is well known that the PN expansion is slowly converging, and higher-order PN terms do not necessarily lead to smaller residuals. In fact, successively higher-order PN terms often lead to partial cancellations. Whilst the 6PN and 7PN terms yield a smaller residual relative to TEOBRESUMS, they also display a turning point at high frequencies for large tidal deformabilities. This introduces additional complexity into the function which can be difficult to accurately fit, often requiring more phenomenological coefficients in the PHENOMGSF ansatz. Therefore, we adopt a 7.5PN baseline as it is the highest-order PN series and yields a monotonic residual across the parameter space, see Fig. 3.

We choose collocation points at Gauss-Chebyshev nodes to reduce fitting errors in comparison to equidistant nodes [36], in which the i^{th} node is placed at

$$f_i = f_{\min} + \frac{f_{\max} - f_{\min}}{2} \left(1 + \cos \left[\frac{i\pi}{n} \right] \right), \quad (4.6)$$

where $\{f_{\min}, f_{\max}\}$ is the frequency range over which the nodes are placed and n is the number of collocation points. We find that five phenomenological coefficients provides an optimal balance between goodness-of-fit and the subsequent computational efficiency of the model. An example of this procedure is shown in Fig 4.

A practical consideration is that the choice of termination frequency dictates the frequency spacing of the collocation points, and the concomitant structure of each phenomenological fit. A choice of a constant termination frequency would correspond to each collocation point lying at the same geometric frequency at every point in the parameter space. This leads to problems for binaries

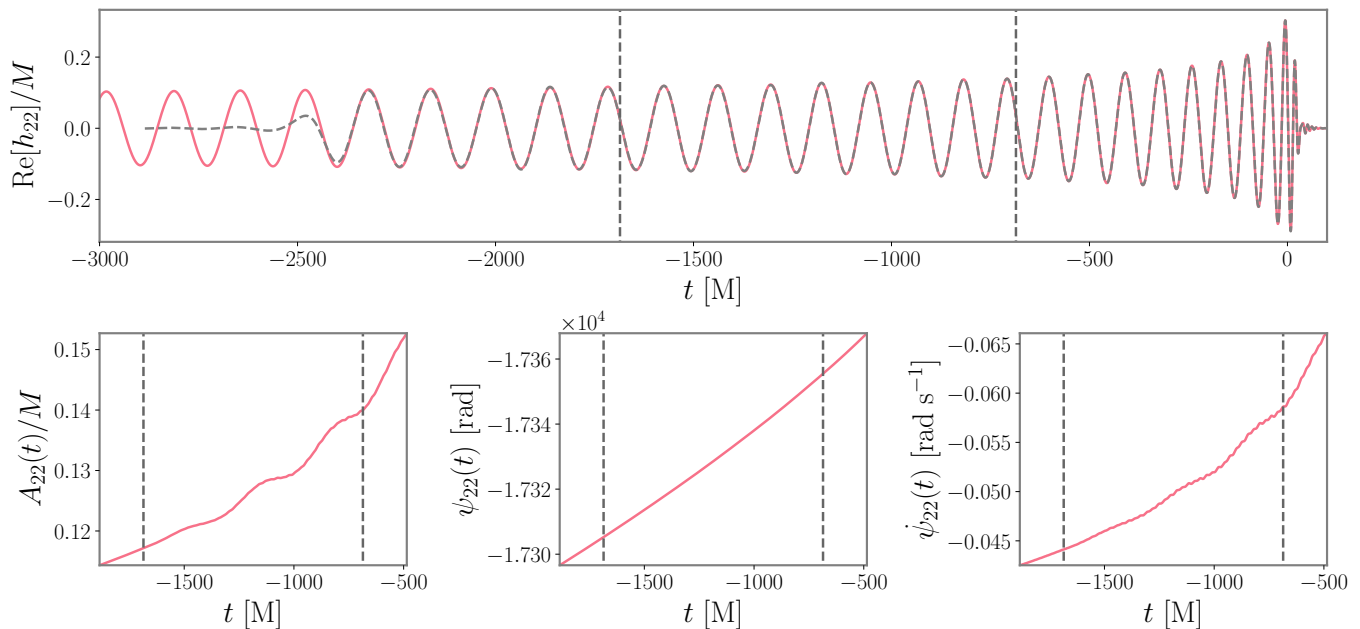


FIG. 2. TEOBRESUMS-NR hybrid example for BAM_0001. *Top panel:* Real part of h_{22} showing the NR data (dashed grey), the aligned TEOBRESUMS waveform (pink) and hybridisation region marked by the two dashed vertical lines. *Bottom panel:* Close ups of the hybridisation region for the resulting hybrid waveform for the amplitude (left), the phase (middle), and the first time derivative of the phase (right).

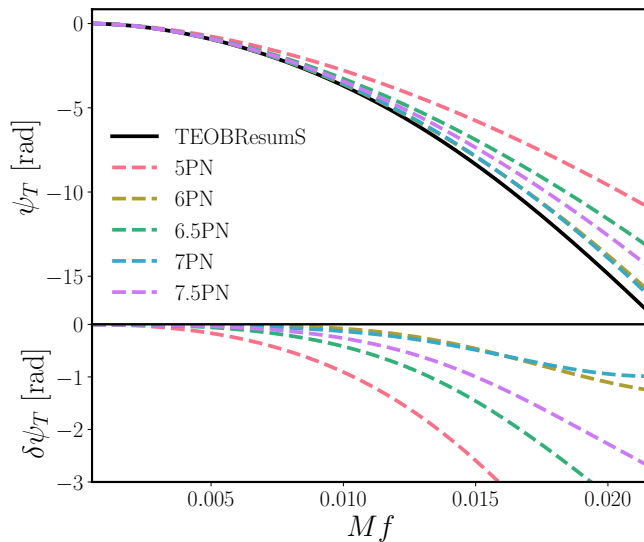


FIG. 3. *Top:* Tidal phase ψ_T as a function of frequency for a binary with parameters $\{q = 1, \Lambda_1 = \Lambda_2 = 600\}$. We show the TEOBRESUMS data (solid black) alongside several TaylorF2 approximants of different PN orders (dashed lines) aligned as per Eq. (4.5). *Bottom:* Phase difference $\delta\psi_T = \psi_T^{\text{TEOB}} - \psi_T^{\text{PN}}$ between between TEOBRESUMS and each Taylor approximant.

with extremely large and extremely small tidal deformabilities, with the relevant morphological features being poorly captured. For example, a termination frequency

that is too high can result in information beyond f_{MECO} being included, where the PN expansion has formally broken down.

To resolve this, one may try to adopt a parameter-space dependent termination frequency, though this often results in a more complex structure to the global fit of the collocation values. One such example is the NR informed contact frequency Mf_{contact} [68], though we find that this leads to a number of subtle issues. First, Mf_{contact} spans a large dynamical range across the parameter space, introducing significant substructure to the fits. Second, we find issues in constructing a fit across the parameter space related to how the frequency smoothly transitions to the black-hole limit and exotic equations-of-state that are outside the calibration regime of Mf_{contact} , especially when $\Lambda_2 > \Lambda_1$.

Overall, we find that the best compromise is the non-spinning hybrid minimum energy circular orbit (MECO) frequency, Mf_{MECO} , introduced in [92]. This spans a comparatively small range of frequencies that are well-behaved and simplify the resulting phenomenological fits. In practice, we use the phenomenological fit for Mf_{MECO} provided in Ref. [36],

$$Mf_{\text{MECO}}(\eta) = \frac{a_0 + a_1\eta + a_2\eta^2 + a_3\eta^3}{1 + b\eta}, \quad (4.7)$$

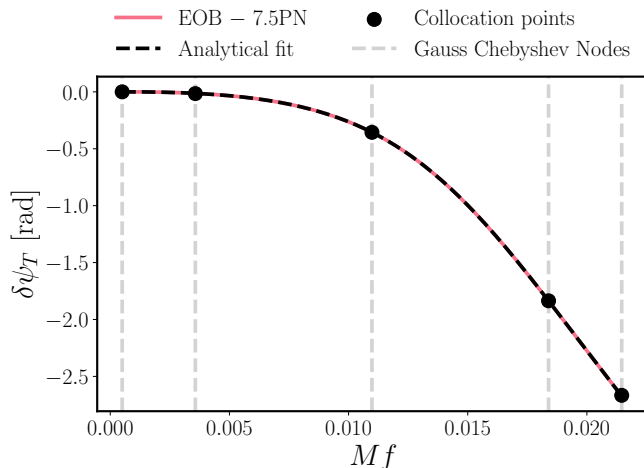


FIG. 4. Example of a tidal residual $\{q = 1, \Lambda_{1,2} = 600\}$ as a function of frequency (pink solid line) with the corresponding analytical fit from a 5th order polynomial (black dashed line). The Gauss-Chebyshev nodes (grey dashed line) are shown alongside their corresponding collocation points (black circles).

with coefficients

$$\begin{aligned} a_0 &= 0.018744, & a_1 &= 0.007790, \\ a_2 &= 0.003940, & a_3 &= -0.000067, \\ b &= -0.104233. \end{aligned}$$

The TEOBRESUMS waveforms are then generated over the frequency interval $\{Mf_{\min}, Mf_{\max}\} = \{0.0005M, Mf_{\text{MECO}}\}$. For a $2M_{\odot}$ binary, the lower frequency limit corresponds to 50Hz, which is significantly below the GW frequency ($\sim 400\text{Hz}$) where tidal effects introduce a measurable phase difference relative to the BBH case [1]. As we do not recalibrate the point-particle sector, we find no practical benefit in going to lower starting-frequencies.

C. Parameter Space Fits

At each collocation point, we construct a fit for the value of the collocation point. This provides a map from $\{\eta, \tilde{\Lambda}, \delta\tilde{\Lambda}\}$ to the value of residual at the collocation node. We explored further reducing the parameter space to $\{\eta, \tilde{\Lambda}\}$, but this resulted in a significant degradation of the accuracy. As such, in this section we only discuss the full 3D fit. Due to the high dimensionality, we adopt a hierarchical approach in which the parameter space fits are constructed dimension-by-dimension [36, 93]. In practice, the starting point is a 1D fit across a well-defined subspace. From this, we can construct the 2D fit by expanding the 1D basis in terms of the second dimension. The complete 3D information is then incorporated by re-expanding the 2D basis in terms of the final dimension. All fits are computed using Mathematica's `NonlinearModelFit` package.

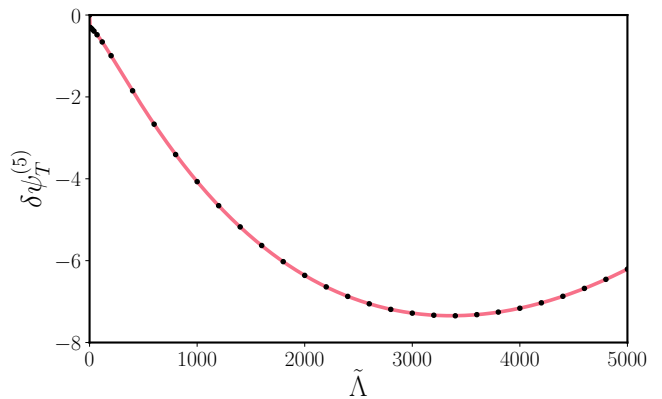


FIG. 5. 1D fit for equal mass ($\eta = 0.25$) systems with $\delta\tilde{\Lambda} = 0$ across $\tilde{\Lambda}$ at the 5th collocation point. The values of the dephasing at this collocation point are shown (black dots), as well as the final Padé fit (pink solid line).

1. 1D Fit

The 1D fit is taken to correspond to the equal mass, $\eta = 0.25$, and equal tidal deformability, i.e. $\delta\tilde{\Lambda} = 0$, subspace. In Fig. 5, we show the dephasing at the fifth collocation point as a function of $\tilde{\Lambda}$. This collocation point corresponds to Mf_{MECO} . We note that there is a notable change in the slope of the fit as $\tilde{\Lambda} \rightarrow 0$ corresponding to the transition from a binary neutron star to a binary black hole, which is related to the minimum tidal deformability enforced in TEOBRESUMS. In practice, we find that such features do not cause significant issues in the fitting procedure and we have verified that the model extrapolates sufficiently smoothly to the binary black hole limit.

We fit polynomial ansatzes against the data up to various orders I

$$F(\eta = 0.25, \tilde{\Lambda}, \delta\tilde{\Lambda} = 0) = \sum_{i=0}^I a_i \tilde{\Lambda}^i, \quad (4.8)$$

where a best fit is defined for the lowest Bayesian Information Criterion (BIC), which attempts to avoid overfitting by adding a penalty for the number of parameters in a given model, e.g. see discussion in [93]. After selecting the best fit, we construct a Padé approximant at a given order, which helps to effectively resum the information,

$$\sum_{i=0}^I a_i \tilde{\Lambda}^i \rightarrow \frac{\sum_{j=0}^J b_j \tilde{\Lambda}^j}{1 + \sum_{k=1}^K c_k \tilde{\Lambda}^k}, \quad (4.9)$$

where $J, K \leq I$. A benefit of using Padé approximants is that they are more robust when extrapolating outside the calibration region than standard Taylor expanded results [94].

As before, we construct a range of Padé approximants with differing orders and use `NONLINEARMODELFIT` to infer the BIC. The residuals and BIC are used to determine the functional form of the final 1D fit.

2. 2D Fit

To obtain the $\{\eta, \tilde{\Lambda}\}$ fit, we expand Eq. (4.9) about η keeping $\delta\tilde{\Lambda} = 0$. The hierarchical process involves inserting a polynomial of order M into the 1D fit via

$$a_l \rightarrow a_l \sum_{m=0}^M b_{lm} \eta^m. \quad (4.10)$$

We only apply this insertion to the numerator of the 1D fit Eq. (4.9) to avoid singularities. To assess the fit quality we found that in the 2D case, the penalty introduced in the BIC is not sufficient to avoid over-fitting. We introduce 3 sets of randomly generated data in the subparameter space $\{\eta, \tilde{\Lambda}, \delta\tilde{\Lambda} = 0\}$ and evaluate the goodness of fit between the independent data and the proposed ansätze. To measure the goodness-of-fit, we use an R^2 criterion

$$R^2 = 1 - \frac{\sum_i (r_i - \hat{r}_i)^2}{\sum_i (r_i - \bar{r}_i)^2}, \quad (4.11)$$

where r_i is the residual fit value, \hat{r}_i is the true value, and \bar{r}_i is the mean. We impose a condition of $1 - R^2 \leq 10^{-3}$, with fits exceeding this tolerance being discarded. Due to the increasing complexity of the higher-order fits, we evaluate the BIC for each fit with the highest-scoring, and therefore lowest contributing factor, being removed. This process is iterated until $1 - R^2$ decreases by at least an order of magnitude. This helps eliminate parameters in the fit that are not contributing and slowing the computation time down. An example of a 2D fit is shown in Fig. 6.

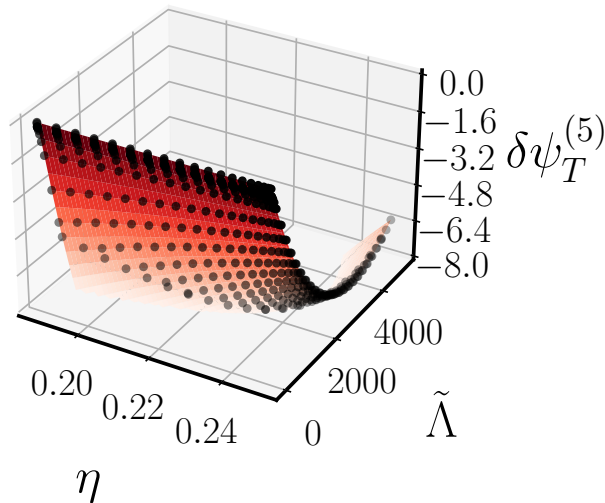


FIG. 6. 2D fit across $\{\eta, \tilde{\Lambda}\}$ for $\delta\tilde{\Lambda} = 0$ at the 5th collocation point. The values of the dephasing at this collocation point are shown (black dots), as well as the final 2D fit (red surface).

3. 3D Fit

This process is then repeated for the full 3D fit, with all input data, covering the full $\eta, \tilde{\Lambda}, \delta\tilde{\Lambda}$ space as detailed in Sec. III. Once again a polynomial of order N is inserted in the numerator

$$a_l b_{lm} \rightarrow a_l b_{lm} \sum_{n=1}^N c_{lmn} \delta\tilde{\Lambda}^n. \quad (4.12)$$

Note here that by definition $\delta\tilde{\Lambda} = 0$ recovers the 2D case. Once again the same R^2 criterion as in the 2D fit is implemented alongside the iterative cutting of c_{lmn} . At this point a full parameter space fit is achieved, full expressions for the 3D fits at each collocation point is given in Appendix A.

D. Inclusion of Spin

Whilst PHENOMGSF is only calibrated to nonspinning data, spin-effects, such as the spin-spin and self-spin tidal terms, can be incorporated into the phase using the PN expressions directly

$$\psi_T = \psi_{\text{BBH}} + \psi_{\text{PhenomGSF}} + \psi_{\text{SS}}. \quad (4.13)$$

Contributions associated to the mass-monopole and spin-dipole are already incorporated in the point-particle phase. We use the PN baseline from [36], which includes all point-particle spin information up to 3.5PN [95, 96]. We subsequently incorporate the equation-of-state dependent quadrupole and octupole terms, which are related to the mass and spin moments via $M_2^{(A,B)} = -C_Q^A M_{A,B}^3 \chi_{A,B}^2$ and $S_3^{(A,B)} = -C_{\text{Oct}}^{A,B} M_{A,B}^4 \chi_{A,B}^3$ respectively. Here C_Q and C_{Oct} parameterize the quadrupolar and octupolar deformations of the stars induced by their spin, e.g. [24, 29, 60, 62, 95–99]. For neutron stars or other exotic compact objects, $C_X \neq 1$ and need to be calculated assuming a given equation-of-state. The self-spin terms can be schematically written as [29]

$$\psi_{\text{SS}} = \frac{3x^{5/2}}{128\nu} \left(\psi_{\text{SS},2\text{PN}}^A x^2 + \psi_{\text{SS},3\text{PN}}^A x^3 + \psi_{\text{SS},3.5\text{PN}}^A x^{7/2} \right), \quad (4.14)$$

where $x = (2\pi/f)^{2/3}$ and the individual coefficients can be found in [29], ensuring that contributions from the black hole multipoles are explicitly removed to avoid double-counting their effect, which is already contained in the point-particle phase.

This extends the model to include partial aligned-spin information, though we note that these contribution are not calibrated within the PHENOMGSF model and therefore not informed by TEOBRESUMS. This is similar to how spin information is incorporated in other models, e.g. [29, 30]. Should we wish to reduce the number of free parameters in the model, we can impose URs that relate C_Q^A and C_{Oct}^A to the tidal deformability Λ_A , e.g. [100].

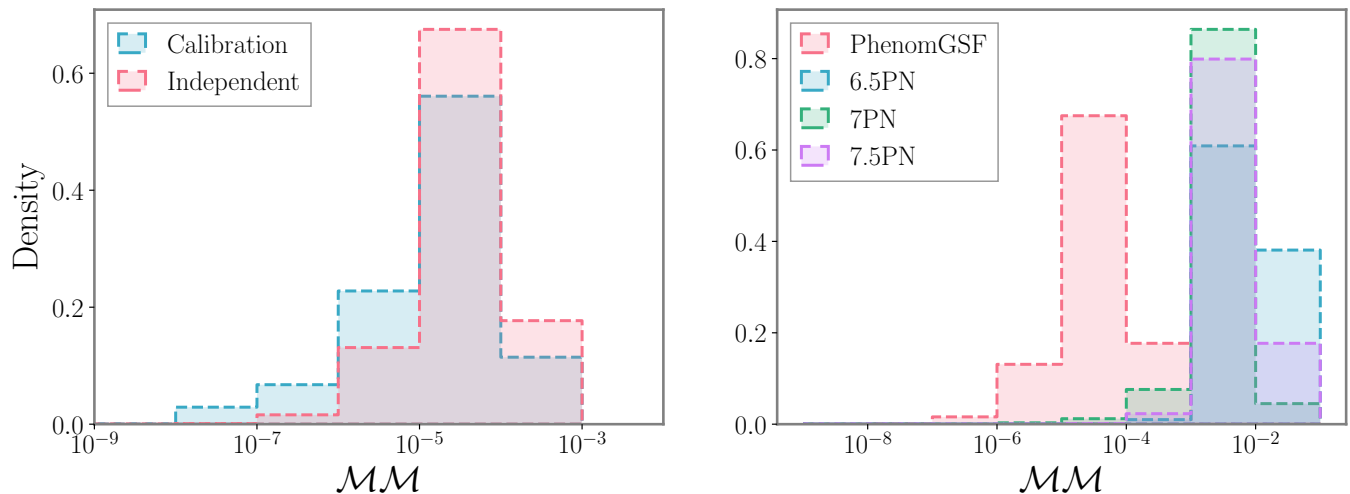


FIG. 7. Mismatches between TEOBRESUMS and several other tidal models. *Left panel:* Mismatches of PHENOMGSF against the calibration data (blue) as well as randomly selected binaries within the calibration region but not seen in the fitting (pink). *Right panel:* Mismatches of PHENOMGSF data (pink), and TAYLORF2 6.5PN (blue), 7PN (green) and 7.5PN (purple) and against TEOBRESUMS.

This is the strategy we employ by default, though the model also allows us to treat C_Q^A and C_{Oct}^A as free EOS-dependent parameters to be constrained by the data.

Model validation including spin is considered in Sec. V to check for consistency. We note that when including the 3.5PN spin-spin term, we do make use of universal relations, which are required to calculate the compactness of each neutron star [55]. Extending this to generic compact objects, such as boson stars, is left to future work. Nonetheless, this is a comparatively small contribution to the phase and as we do not impose universal relations between the mass and tidal deformability, we do not expect this to have a significant impact. If desired, the spin-spin contributions in PHENOMGSF can be disabled, given the modularity and flexibility of the framework.

V. MODEL VALIDATION

To assess the accuracy of PHENOMGSF we perform several mismatch comparisons as well as full Bayesian parameter estimation.

A. Mismatch Comparisons

To assess how similar two waveforms are, we compute the match \mathcal{M} defined as the time- and phase-optimised noise-weighted inner product between two waveforms given by

$$\mathcal{M}(h_1, h_2) = \max_{t_0, \phi_0} \frac{\langle h_1, h_2 \rangle}{\sqrt{\langle h_1, h_1 \rangle \langle h_2, h_2 \rangle}}, \quad (5.1)$$

where

$$\langle h_1 | h_2 \rangle = 4\Re \int_{f_{\min}}^{f_{\max}} \frac{\tilde{h}_1(f) \tilde{h}_2^*(f)}{S_n(f)} df, \quad (5.2)$$

where $S_n(f)$ denotes the one-sided power spectral density (PSD) of the detector noise, \tilde{h} the Fourier transform of h and $*$ complex conjugation. For a detector agnostic approach, we choose white noise, i.e. $S_n(f) = 1$. The *mismatch* $\mathcal{M}\mathcal{M}$ is then defined as

$$\mathcal{M}\mathcal{M}(h_1, h_2) \equiv 1 - \mathcal{M}. \quad (5.3)$$

To compute mismatches, we first need to construct complete waveforms h_1, h_2 . We choose the TEOBRESUMS BBH phase, the TEOBRESUMS BNS amplitude and vary the choice of tidal phase. Therefore, in all mismatches shown the only difference is the tidal phase allowing for a direct comparison.

The left panel of Fig. 7 shows histograms of the mismatches between TEOBRESUMS and PHENOMGSF for the 8446 waveforms used in the model calibration, and 1000 independent waveforms that lie within the model's calibration range but were not used in the fitting. The mismatches in both data sets are $\mathcal{M}\mathcal{M} \leq 10^{-3}$, with a median mismatch of $\sim 2 \times 10^{-5}$ for the calibration dataset and $\sim 3 \times 10^{-5}$ for the independent dataset, which quantifies the average modelling error. We also see excellent agreement between the two distributions, with a tail towards lower mismatches, demonstrating that the PHENOMGSF model is robust and not overfitted. The improvement of PHENOMGSF over TAYLORF2 at different PN orders is shown in the right panel of Fig. 7. Here we find that the agreement between PHENOMGSF and TEOBRESUMS is on average ~ 3 orders of magnitude better than with any of the considered PN approximants.

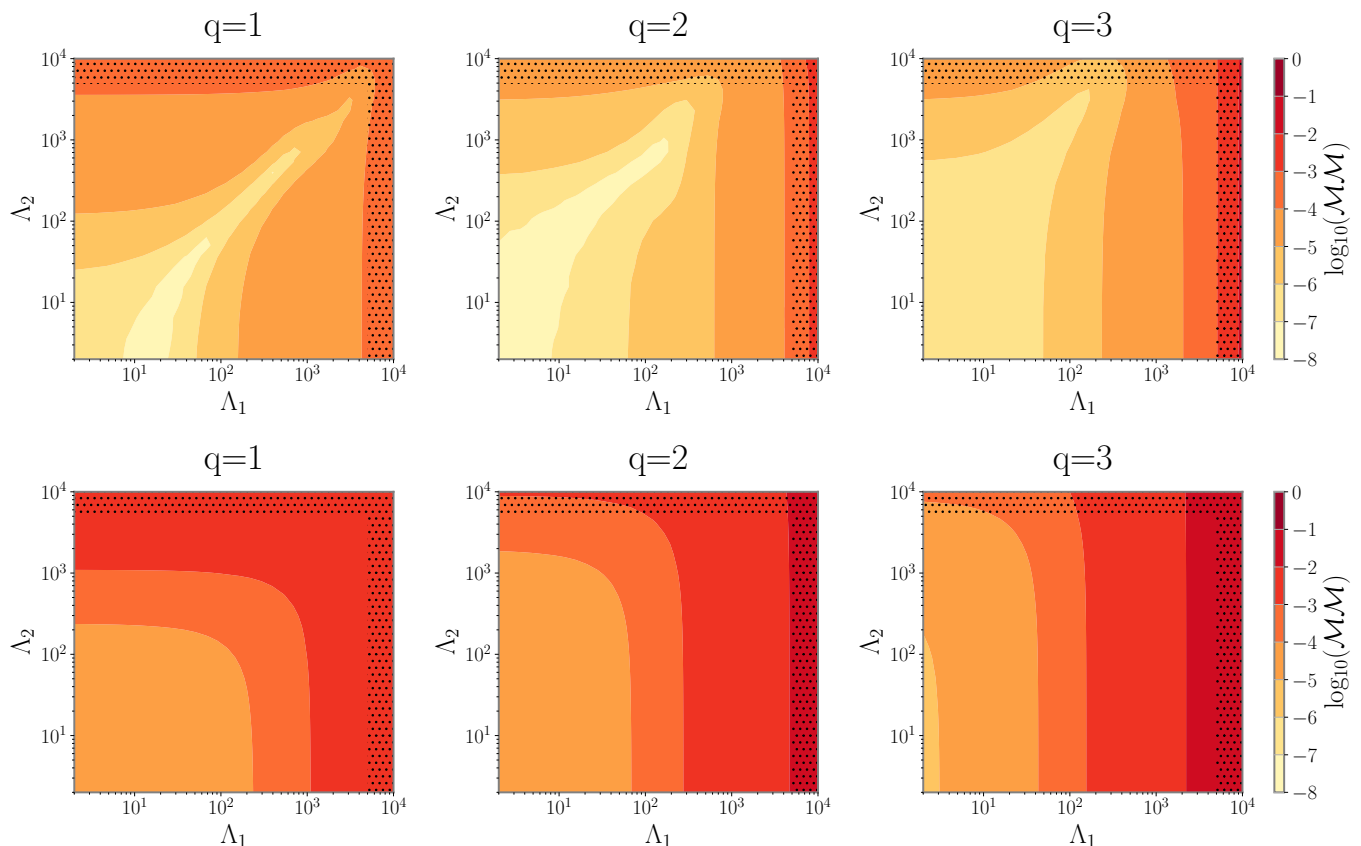


FIG. 8. Mismatches across the parameter space over $Mf = [0.0005, Mf_{\text{MECO}}]$ at $q = 1, 2$ and $q = 3$. The dotted areas denote regions of parameter space outside the calibration range of the model. *Top row*: Mismatches between TEOBRESUMS and PHENOMGSF. *Bottom row*: Mismatches between TEOBRESUMS and TAYLORF2 at 7.5PN.

In Fig. 8 we show how the mismatches of TEOBRESUMS against PHENOMGSF (top row) and TAYLORF2 with 7.5PN tides (bottom row) vary as a function of $\{\Lambda_1, \Lambda_2\}$ for $q = 1, 2, 3$. Here, we also include waveforms outside the calibration region of PHENOMGSF to test for the robustness of the model under extrapolation to $\Lambda_{1,2} \leq 10000$ (dotted regions). We find that the PHENOMGSF mismatches degrade for more unequal-mass systems, although they remain $< 10^{-3}$ throughout the calibration range. We note that in the equal-mass limit the mismatches are not fully symmetric in the $\Lambda_1 - \Lambda_2$ plane, even though the input data is symmetric under the interchange $1 \leftrightarrow 2$. This is due to the fact that in the fitting procedure, we did not enforce this symmetry in the equal-mass limit. Nonetheless, the mismatches in this regime are negligible and of the order $\sim \mathcal{O}(10^{-7})$. The asymmetry observed for unequal masses is as expected. In contrast, tidal TAYLORF2 performs significantly worse even for moderate parameters, exceeding mismatches of 10^{-3} for $\Lambda_{1,2} \gtrsim 1000$ at $q = 1$, and $\Lambda_1 \gtrsim 100$ for $q = 3$. We observe better agreement within the regions nominally consistent with hadronic EOSs: For example, for equal masses $\Lambda_1 = \Lambda_2$ gives the lowest mismatches, and for unequal mass ratios the lowest mismatches are found for $\Lambda_2 > \Lambda_1$.

Outside the calibration region, PHENOMGSF achieves mismatches $< 10^{-3}$ for equal-mass binaries; for $q = 3$, mismatches remain below 10^{-3} for $\Lambda_2 < 10000$ provided that $\Lambda_1 < 5000$ but start to degrade significantly for larger values of Λ_1 . We note, however, that this requires the radius of the primary neutron star to be ~ 2.6 times larger than that of the secondary.

Finally, we quantify the model's accuracy by also computing mismatches against a selection of TEOBRESUMS-NR hybrid waveforms as detailed in Sec. III C. In Fig. 9 we show comparisons against TEOBRESUMS, PHENOMGSF and NRTIDALV2. We note that the NRTIDALV2 model is the only tidal phase model in this comparison that is calibrated to NR simulations. Hence, we expect this model to have better agreement with the hybrids close to merger. At low frequencies, however, we expect PHENOMGSF to yield dephasing results similar to those of TEOBRESUMS by construction. The top two panels of Fig. 9 are for equal-mass nonspinning systems, the middle two for unequal mass nonspinning systems, and the bottom two are for equal-mass systems with aligned spins. For each panel, the top figure shows the mismatch where $f_{\text{min}} = 40$ Hz to varying f_{max} up to a maximum of $f_{\text{max}} = f_{\text{MECO}}$, while the bottom shows the phase difference as a function of GW frequency.

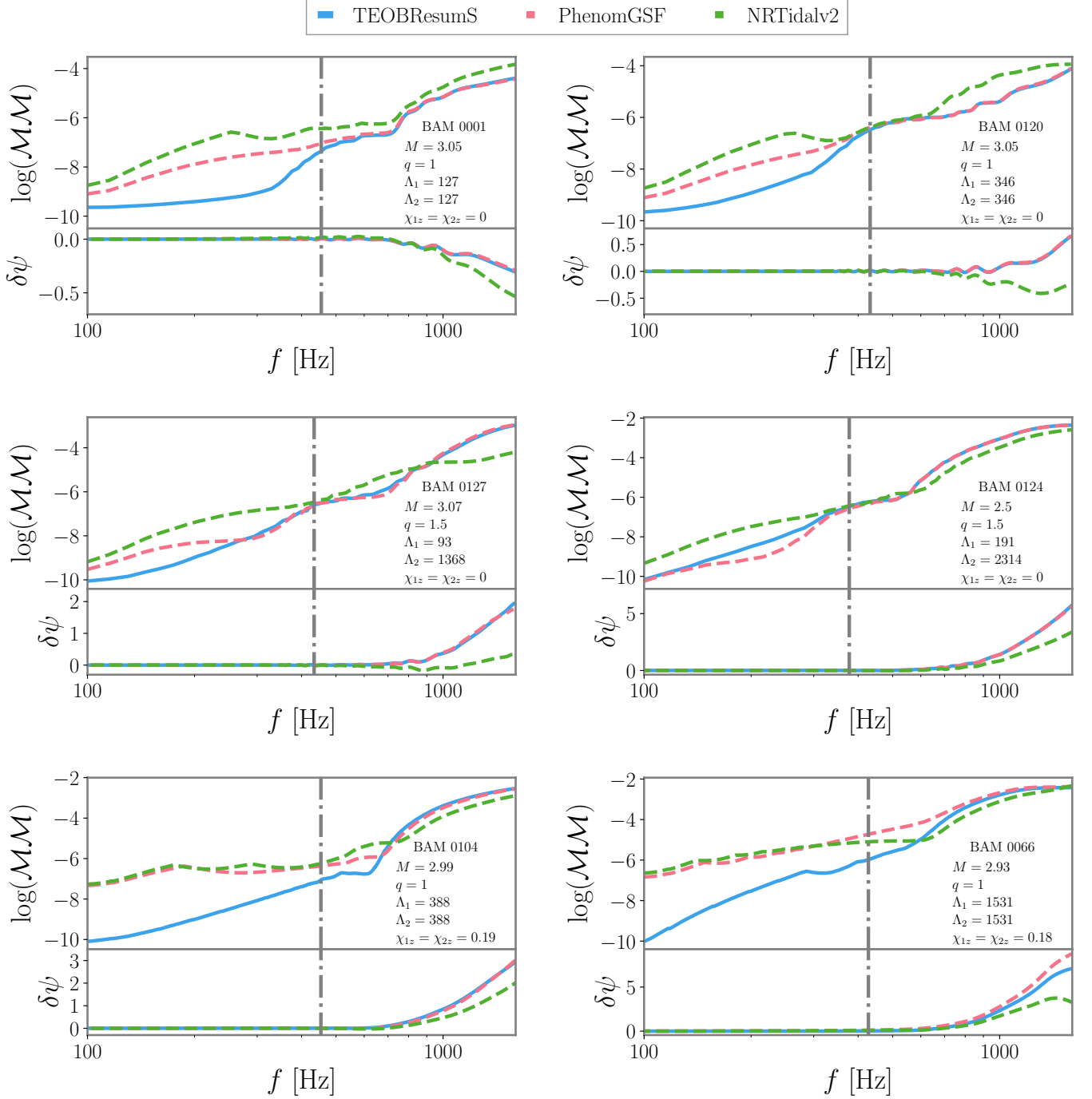


FIG. 9. Comparisons for TEOBRESUMS-NR hybrid waveforms against TEOBRESUMS (blue solid), PHENOMGSF (orange dashed) and NRTIDALV2 (green dashed). In each plot the upper panel shows \log mismatches computed from 40 Hz to a maximum frequency f ; the lower panel shows the dephasing between the NR hybrid and one of the tidal approximants, i.e. $\delta\psi = \psi_{NR} - \psi_X$ where X is one of the approximants. The NR starting frequency is marked by the grey dot-dashed line. *Top row*: Equal-mass nonspinning systems. *Middle row*: Unequal mass nonspinning systems. *Bottom row*: Equal-mass spinning systems. The details of the NR simulations are given in Tab. I.

As anticipated, PHENOMGSF tracks the phase of TEOBRESUMS to a very high degree. The only notable phase difference between PHENOMGSF and TEOBRESUMS is seen for BAM 0066. In all cases, except for

the equal-mass nonspinning hybrids, NRTIDALV2 gives the smallest dephasing for the NR portion of the hybrid waveforms. The observed oscillations in the dephasing are due to non-negligible residual eccentricities in the

NR initial data (see Tab. I). For the mismatches we find that for all comparisons the PHENOMGSF results consistently approach those of TEOBRESUMS around or after the NR starting frequency indicated by the vertical line. The mismatches seemingly disagree at lower frequencies, however, we note that this difference is $\sim \mathcal{O}(10^{-10})$ for the nonspinning cases and $\sim \mathcal{O}(10^{-7})$ for the spinning cases. Surprisingly, for the equal mass non-spinning cases (top row) we find that PHENOMGSF performs better than NRTIDALV2 across the entire frequency range. For the unequal mass cases, PHENOMGSF obtains lower mismatches in the low-frequency region, however, in the high frequency regime NRTIDALV2 performs better. For the spinning comparisons we find that PHENOMGSF and NRTIDALV2 are comparable for low frequencies, while TEOBRESUMS is by far the most faithful. When including the NR region, all three models are comparable with NRTIDALV2 being slightly better than the other two models.

B. Parameter Estimation

To further validate PHENOMGSF we carry out full Bayesian inference on simulated nonspinning and aligned-spin PHENOMXAS_PHENOMGSF signals (injections), a TEOBRESUMS-NR hybrid waveform, and GW170817 data [101].

The posterior density distribution function (PDF) of a set of model parameters θ given the data d is

$$p(\theta|d) = \frac{\mathcal{L}(d|\theta)\pi(\theta)}{\mathcal{Z}_d}, \quad (5.4)$$

where $\mathcal{L}(d|\theta)$ denotes the likelihood, $\pi(\theta)$ the prior, and \mathcal{Z}_d the evidence or marginalised likelihood which is defined as

$$\mathcal{Z}_d = \int \mathcal{L}(d|\theta)\pi(\theta)d\theta. \quad (5.5)$$

For our analyses, we consider the following model parameters: $\theta = \{\mathcal{M}_c, q, \chi_1, \chi_2, \tilde{\Lambda}, \delta\tilde{\Lambda}, \text{RA}, \text{DEC}, \theta_{jn}, \psi, \phi, t_c\}$, where $\mathcal{M}_c = (m_1 m_2)^{3/5} / M^{1/5}$ denotes the chirp mass, q the mass ratio, χ_1 and χ_2 the two spin magnitudes for the aligned-spin runs, RA and DEC the right ascension and declination of the binary in the sky, ψ the polarisation angle, ϕ and t_c the phase and time of coalescence respectively, and θ_{jn} the inclination of the total angular momentum w.r.t. to the line-of-sight. The luminosity distance D_L and phase ϕ are marginalised over in the likelihood evaluation and reconstructed in post-processing. All runs were performed with BILBY [102] in conjunction with the nested sampler DYNESTY [103] with slice sampling. For all analyses we used 2000 live points, 20 slices and 50 autocorrelation lengths with 32 CPU cores. Although we sample in \mathcal{M}_c and q , we select priors that are uniform in component masses,

whilst $\tilde{\Lambda}$ and $\delta\tilde{\Lambda}$ are sampled directly from uniform priors. The priors for each analysis are given in Tabs. II and III. Additionally, we constraint the individual tidal deformabilities Λ_1, Λ_2 to be between 0 and 5000.

1. Zero-Noise Injections

We first perform two zero-noise injections with IMRPHENOMXAS_PHENOMGSF into a three-detector network consisting of LIGO-Hanford, LIGO-Livingston [104] and Virgo [105] (HLV) with the sensitivity of the fourth observing run (O4) [106] and recover with the same model. We note that zero-noise is representative of the results when averaging over many different noise realisations. The frequency-dependence of the sensitivity is taken into account through the PSD. The injected parameters are similar to those of GW170817 (see Tab. II for details). For the EOS we choose the relatively soft APR4 [107] one, which is compatible with the EOS-constraints obtained from GW170817 [10, 108]. We perform two analyses: one with zero NS spin and another one with aligned-spins of magnitudes $\chi_1 = \chi_2 = 0.01$. We integrate the likelihood from a minimum frequency $f_{\min} = 23$ Hz to $f_{\max} = 2048$ Hz, which corresponds to the Nyquist frequency of our sampling rate. Although PHENOMGSF is only calibrated from a minimum frequency of 37 Hz for such a GW170817-like system, we have confirmed that extrapolating to lower frequencies is robust due to the nature of our ansatz. Both configurations have a network signal-to-noise ratio (SNR) of ~ 97 .

A selection of 1D and 2D posterior distributions for the nonspinning injection is shown in Fig. 10. We find that for all parameters the injected values lies confidently within the 90% credible interval. As expected, $\tilde{\Lambda}$ is recovered with better accuracy than $\delta\tilde{\Lambda}$ as it is the leading-order tidal contribution to the GW phase, while $\delta\tilde{\Lambda}$ is subdominant. We also observe the expected linear correlation between the chirp mass and $\tilde{\Lambda}$. Mapping the binary tidal parameters to the individual tidal deformabilities, we observe the known correlation between the two and recover the injected values at the 50% credible level as can be seen in the right panel of Fig. 10. The median values and 90% credible intervals for all parameters are given in the fourth column of Tab. II.

In Fig. 11 we show a similar selection of 1D and 2D posteriors for the aligned-spin analysis, but now also including the effective spin χ_{eff} [33]. We find that the chirp mass and tidal parameters are recovered equally accurately as in the nonspinning case, but we now observe the known non-linear correlation between the mass ratio and the effective spin [109, 110], pushing the mass ratio posterior towards more equal masses for low spin magnitudes. The tidal parameters are, however, still recovered well. The median values and 90% credible intervals for all parameters are given in the fifth column of Tab. II.

Parameter	Injected Value	Prior	Nonspinning	Aligned-Spin
$\mathcal{M}_c [M_\odot]$	1.20	$U_{(m_1, m_2)}[\mathcal{M}_{\min}, \mathcal{M}_{\max}]$	$1.20 \pm_{2.17 \times 10^{-5}}^{2.17 \times 10^{-5}}$	$1.20 \pm_{3.20 \times 10^{-5}}^{4.34 \times 10^{-5}}$
q	0.86	$U_{(m_1, m_2)}[0.125, 1.0]$	$0.86 \pm_{0.02}^{0.03}$	$0.89 \pm_{0.13}^{0.10}$
$\tilde{\Lambda}$	293.5	$U[0, 5000]$	$296 \pm_{59}^{62}$	$290 \pm_{60}^{61}$
$\delta\tilde{\Lambda}$	34.7	$U[-5000, 5000]$	$19 \pm_{112}^{108}$	$10 \pm_{103}^{112}$
χ_1	NA/0.01	NA/ $U[0, 0.05]$	NA	$0.01 \pm_{0.01}^{0.02}$
χ_2	NA/0.01	NA/ $U[0, 0.05]$	NA	$0.01 \pm_{0.01}^{0.02}$
RA [rad]	2.55	$U[0, 2\pi]$	$2.55 \pm_{0.01}^{0.01}$	$2.55 \pm_{0.01}^{0.01}$
DEC [rad]	-0.40	Sine	$-0.41 \pm_{0.01}^{0.01}$	$-0.41 \pm_{0.01}^{0.01}$
D_L [Mpc]	40	$U[0, 2\pi]$	$35 \pm_3^5$	$35 \pm_3^5$
θ_{jn} [rad]	0.1	Sine	$0.52 \pm_{0.37}^{0.35}$	$0.52 \pm_{0.38}^{0.35}$
ϕ [rad]	0	$U[0, 2\pi]$	$3.16 \pm_{2.86}^{2.79}$	$3.16 \pm_{2.86}^{2.79}$
ψ [rad]	0	$U[0, \pi]$	$1.63 \pm_{1.45}^{1.37}$	$1.66 \pm_{1.47}^{1.34}$
t_c [s]	0	$U[-0.005, 0.005]$	$t_c \pm_{1.7 \times 10^{-4}}^{1.8 \times 10^{-4}}$	$t_c \pm_{1.8 \times 10^{-4}}^{1.8 \times 10^{-4}}$

TABLE II. Injected parameters for a nonspinning and aligned spin GW170817-like system with the corresponding prior ranges and recovered values. Here $U_{(m_1, m_2)}$ denotes that the prior is conditional on the detector-frame component masses and we set $\mathcal{M}_{\min} = \mathcal{M}_{c, \text{inj}} - 10^{-3}$ and $\mathcal{M}_{\max} = \mathcal{M}_{c, \text{inj}} + 10^{-3}$. The recovered values denote the median and 90% credible interval. NA indicates that a parameter was not applicable to the nonspinning analysis.

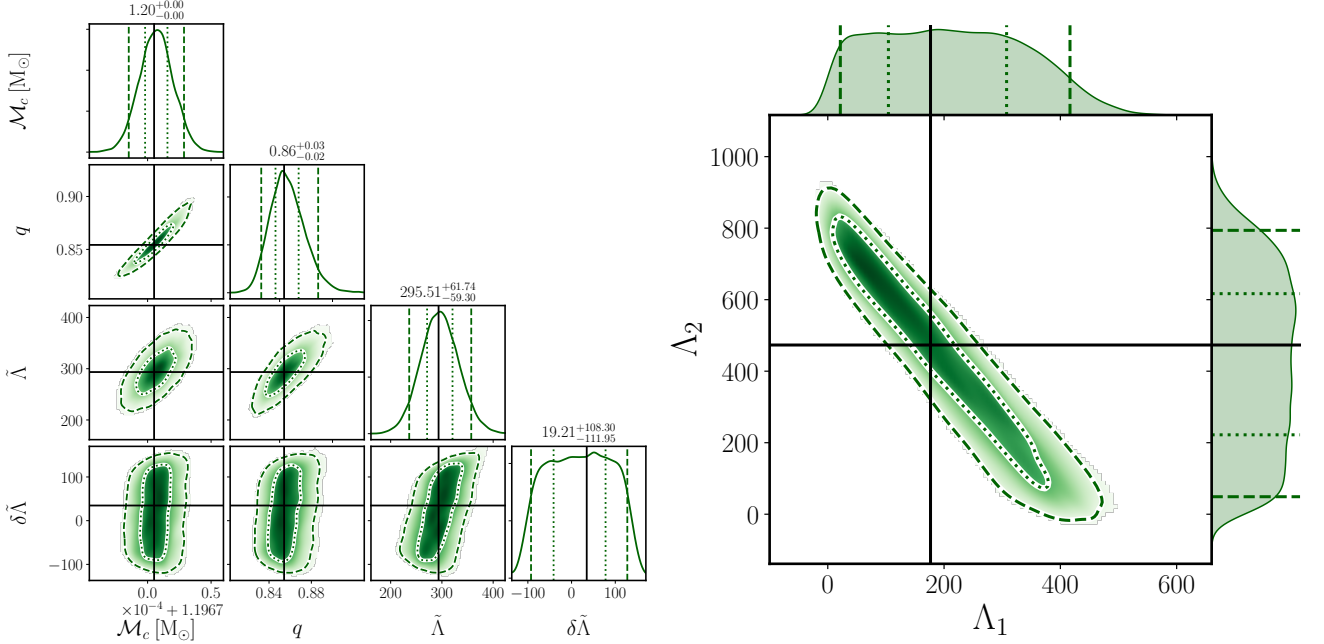


FIG. 10. 1D and 2D posteriors for a nonspinning GW170817-like IMPPHENOMXAS_PHENOMGSF injection. *Left panel:* Posteriors of the intrinsic parameters with their 50% (dotted) and 90% confidence intervals (dashed). The injected values are indicated by solid black lines. *Right panel:* Posteriors for the individual tidal deformabilities with their 50% (dotted) and 90% confidence intervals (dashed).

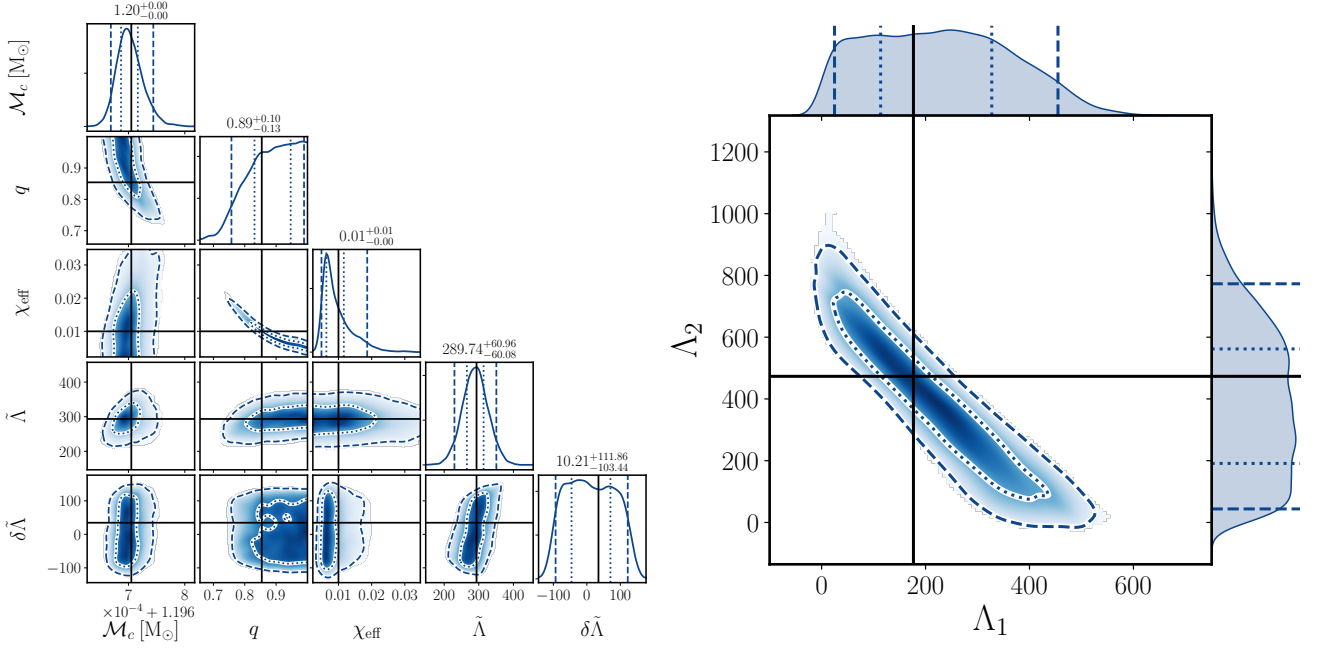


FIG. 11. 1D and 2D posteriors for an aligned-spin GW170817-like IMPPHENOMXAS_PHENOMGSF injection. *Left panel:* Posteriors of the intrinsic parameters with their 50% (dotted) and 90% confidence intervals (dashed). The injected values are indicated by solid black lines. *Right panel:* Posteriors for the individual tidal deformabilities with their 50% (dotted) and 90% confidence intervals (dashed).

Parameter	TEOBResums-NR hybrid			GW170817	
	Injected Value	Prior	Recovered	Prior	Inferred
$\mathcal{M}_c [M_\odot]$	1.18	$U_{(m_1, m_2)} [1.1, 1.3]$	$1.18 \pm_{5.74 \times 10^{-5}}^{3.28 \times 10^{-5}}$	$U_{(m_1, m_2)} [1.197, 1.198]$	$1.1976 \pm_{1.07 \times 10^{-4}}^{1.25 \times 10^{-4}}$
q	1.0	$U_{(m_1, m_2)} [0.125, 1]$	$0.94 \pm_{0.08}^{0.05}$	$U_{(m_1, m_2)} [0.125, 1]$	$0.86 \pm_{0.16}^{0.13}$
$\tilde{\Lambda}$	390	$U[0, 5000]$	$371 \pm_{115}^{104}$	$U[0, 5000]$	$410 \pm_{237}^{516}$
$\delta \tilde{\Lambda}$	0	$U[-5000, 5000]$	$-1 \pm_{133}^{152}$	$U[-5000, 5000]$	$18 \pm_{205}^{207}$
χ_1	0	NA	NA	$U[0, 0.05]$	$0.007 \pm_{0.01}^{0.02}$
χ_2	0	NA	NA	$U[0, 0.05]$	$0.007 \pm_{0.01}^{0.02}$
RA [rad]	2.55	$U[0, 2\pi]$	$2.55 \pm_{0.01}^{0.01}$	$U[0, 2\pi]$	$3.42 \pm_{0.03}^{0.03}$
DEC [rad]	-0.41	Cosine	$-0.41 \pm_{0.02}^{0.02}$	Cosine	$-0.40 \pm_{0.06}^{0.06}$
D_L [Mpc]	40	$U[10, 100]$	$36 \pm_8^5$	$U[10, 100]$	$37 \pm_{16}^8$
θ_{jn} [rad]	0.1	Sine	$2.64 \pm_{0.35}^{0.36}$	Sine	$2.53 \pm_{0.51}^{0.44}$
ϕ [rad]	0	$U[0, 2\pi]$	$2.96 \pm_{2.67}^{2.96}$	$U[0, 2\pi]$	$3.17 \pm_{2.93}^{2.81}$
ψ [rad]	0	$U[0, \pi]$	$1.63 \pm_{1.48}^{1.37}$	$U[0, \pi]$	$1.53 \pm_{1.44}^{1.49}$
t_c [s]	1187008882.4	$U[t_c - 0.1, t_c + 0.1]$	$t_c \pm_{4.3 \times 10^{-4}}^{3.9 \times 10^{-4}}$	$U[t_c - 0.1, t_c + 0.1]$	$t_c \pm_{0.9 \times 10^{-3}}^{1.1 \times 10^{-3}}$

TABLE III. Injected parameters for the TEOBRESUMS-NR hybrid with the corresponding priors and 1D posterior medians with their 90% credible intervals, and priors as well as the median inferred parameter values with their 90% credible intervals for the GW event GW170817. Here, $U_{(m_1, m_2)}$ denotes uniform priors in component masses, and $t_c = 1187008882.4$ s is the GPS time of GW170817. NA indicates that a parameter was not applicable to the nonspinning analysis.

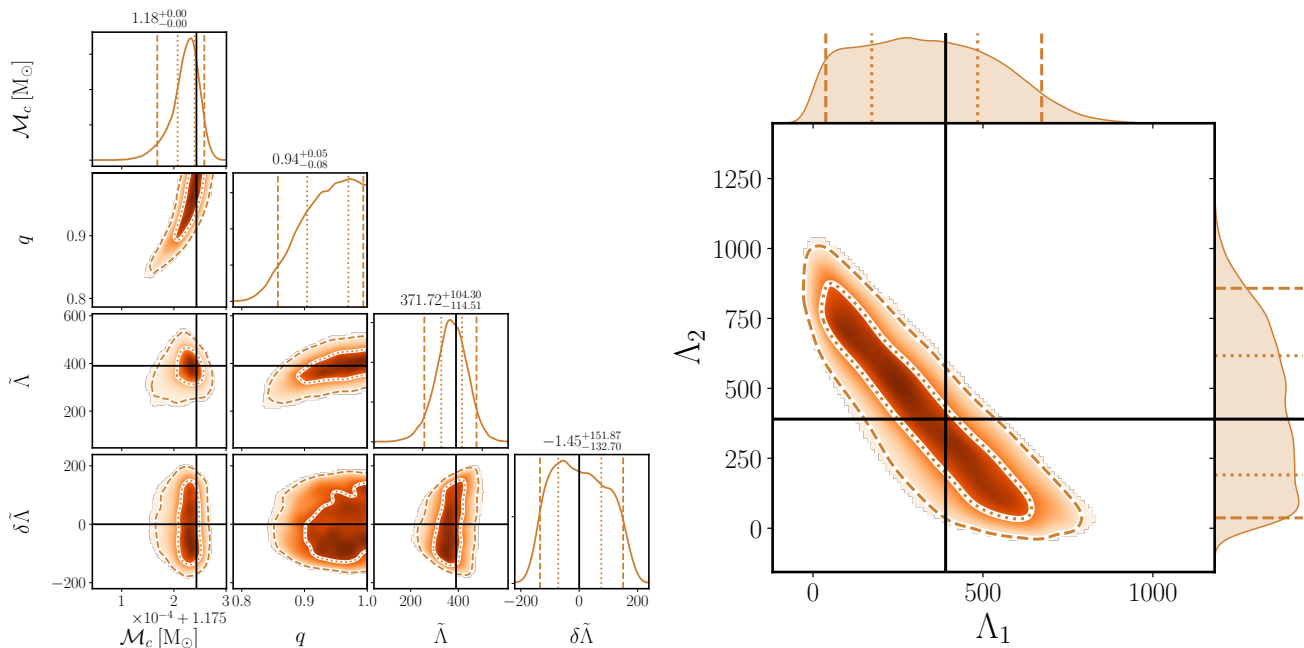


FIG. 12. 1D and 2D posteriors for the TEOBRESUMS-NR hybrid injection with BAM 0095 analysed with IMPPHENOMXAS_PHENOMGSF. *Left panel:* Posteriors of the intrinsic parameters with their 50% (dotted) and 90% confidence intervals (dashed). The injected values are indicated by solid black lines. We note that the injected mass ratio is $q = 1$ and hence overlaps with the plot axis. *Right panel:* Posteriors for the individual tidal deformabilities with their 50% (dotted) and 90% confidence intervals (dashed).

2. TEOBRESUMS-NR Hybrid Injection

Next, we perform a TEOBRESUMS-NR hybrid zero-noise injection into the same HLV network and recover again with IMPPHENOMXAS_PHENOMGSF. For this analysis we use the BAM 0095 simulations. Details on the hybrid generation are given in Sec. III C. The hybrid starting frequency is $f_{\min} = 30$ Hz, while the NR starting frequency is $f_{\text{NR}} = 433$ Hz. To perform the analysis, we convert the hybrid into the LVK-NR format [111] and use the tools provided by the LIGO Algorithms Library [112]. Starting at $f_{\min} = 33$ Hz, we obtain a network SNR of ~ 51 with the O4 design sensitivity, where the extrinsic parameters are the same as for the previous injections. We note that as this is a nonspinning injection, we set the spins to zero in the recovery. The injected values, prior choices and recovered values are given in Tab. III.

In Fig. 12 we show the obtained 1D and 2D posterior distributions for the chirp mass, mass ratio and tidal deformability parameters. We find that despite the differences in the BBH baseline and the lack of NR calibration of PHENOMGSF, all injected values are recovered accurately and contained within either the 90% or even the 50% credible interval, indicating that modelling systematics due to the BBH baseline and the lack of NR calibration are subdominant in this region of the parameter space.

3. GW170817

Finally, we analyse the data of GW170817 with PHENOMGSF again using IMPPHENOMXAS as the BBH baseline model. We follow previous analyses [4, 113] and employ a low-spin prior. Details for all priors are given in the fifth column of Tab. III. We analyse 128 s of data around the trigger time with a sampling rate of 4096 Hz. For the likelihood integration we choose a minimum frequency $f_{\min} = 23$ Hz consistent with the analyses presented in GWTC-1.

The inferred posterior distributions for the masses and tidal deformability are shown in Fig. 13; the results for all other parameters are shown in Fig. 14 in the Appendix. For comparison, we also show the posteriors obtained with the waveform model IMPPHENOMPV2_NRTIDAL from the GWTC-1 analysis [113, 114] as well as posteriors from an analysis identical to ours but with the model IMPPHENOMXAS_NRTIDALV2. The GWTC-1 analysis used flat priors in Λ_1 and Λ_2 , hence our posteriors for $\tilde{\Lambda}$ has been reweighted to a flat $\tilde{\Lambda}$ -prior as used in our setup.

Overall, we observe a very high degree of consistency between the three results. The component mass posteriors show excellent agreement between all three models, with a slightly higher 90% upper bound for PHENOMGSF. Similarly for the tides, where we also find a slightly higher value of $\tilde{\Lambda}$ with PHENOMGSF than what was found in GWTC-1. This is also consistent with the analysis using TEOBRESUMS presented in Ref. [115].

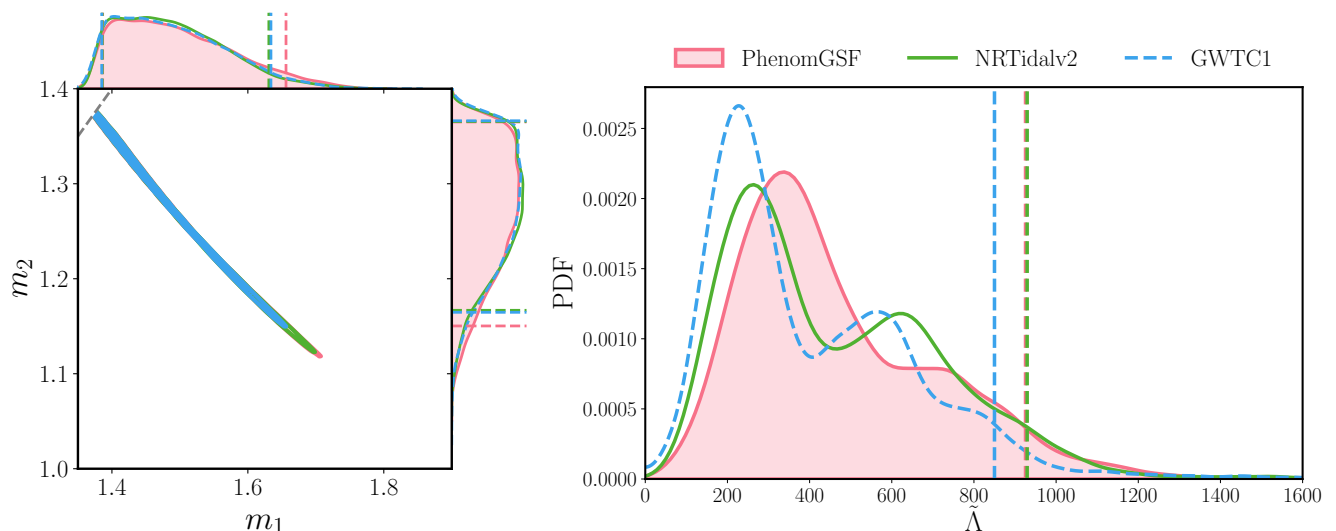


FIG. 13. Selection of 1D and 2D posterior distributions for GW170817 for IMRPHENOMXAS_PHENOMGSF (pink, solid), IMRPHENOMXAS_NRTIDALV2 (green, solid) and IMRPHENOMPv2_NRTIDALV2 (blue, dashed) from GWTC-1. *Left panel:* Component mass posteriors with their 1D 90% credible intervals (vertical dashed lines) and 90% credible region, respectively. Joint 2D posteriors are. The grey dashed line indicates the equal-mass limit. *Right panel:* 1D posteriors for the binary tidal deformability $\tilde{\Lambda}$ with their respective 95th percentiles (vertical dashed lines).

Notably, however, it also appears that the secondary peak in the $\tilde{\Lambda}$ posterior is reduced in comparison to the other models, suggesting that this feature is likely inherent to this generation of NRTIDAL approximants or the previously used BBH baselines. We note that both of these observations are also in agreement with the recent analysis of GW170817 with NRTIDALV3 presented in Fig. 16 of Ref. [30].

VI. DISCUSSION

We presented PHENOMGSF, a new phenomenological tidal phase model for inspiralling unequal mass BNS systems valid for mass ratios between 1 and 3 and dimensionless neutron star tidal deformabilities up to 5000. PHENOMGSF is a closed-form phenomenological fit to the tidal phase of the effective-one-body model TEOBRESUMS, which includes GSF-informed tides. The fit is constructed by employing a hierarchical procedure using the collocation point method to a large suite of TEOBRESUMS waveforms.

PHENOMGSF is fully modular and can readily be added to any frequency-domain BBH baseline model, such as the state-of-the-art IMRPHENOMX waveform family.

We note that we did not include EOB-calibrated spin effects in PhenomGSF, instead relying on standard PN spin-tidal expressions. Whilst we could have assumed an EOS or imposed URs, this is not explicitly required.

We assessed the accuracy and performance of PHENOMGSF extensively by comparing it against independent TEOBRESUMS waveforms, obtaining mismatches

$\mathcal{M}\mathcal{M} \leq 10^{-3}$ across the parameter space the model was calibrated against. For $q \sim 1$ we find that the model extrapolates well and retains its accuracy for tidal deformabilities up to 10000. We also computed frequency-dependent mismatches against a suite of TEOBRESUMS-NR hybrid waveforms, finding that PHENOMGSF tracks the accuracy of TEOBRESUMS as expected.

Finally, we performed full Bayesian inference on a suite of mock signals and the GW event GW170817. Parameter estimation on IMRPHENOMXAS_PHENOMGSF injections into zero-noise show consistent recovery of the injected parameters. We then analyse a TEOBRESUMS-NR hybrid injection and find that neither the lack NR calibration of PHENOMGSF nor the difference in the underlying BBH baseline lead to any significant systematic differences. A more systematic Bayesian study across a wider parameter space is left for future work. Lastly, we independently analyses the data of GW170817 with IMRPHENOMXAS_PHENOMGSF. Our results are consistent with previous analysis, but we obtain a slightly higher upper limit for $\tilde{\Lambda}$ than for example with NRTIDAL and NRTIDALV2. We also found that the secondary peak in $\tilde{\Lambda}$ is less pronounced for PHENOMGSF consistent with the TEOBRESUMS results of GWTC-1. The computational efficiency is comparable to that of the NRTIDAL approximants.

We have demonstrated that PHENOMGSF is a robust, highly accurate, modular and computationally efficient model of quadrupolar gravitoelectric tides. Moreover, it is flexible in that it allows for the addition of PN spin terms and the use of non-hadronic EOS, making it an ideal candidate for exploring exotic matter. Nevertheless, there are several avenues for further improving the model

which we leave for future work, including:

1. A full treatment of neutron star spin effects, extending the 3-dimensional phenomenological fit presented here to higher dimensions to incorporate aligned-spin and precessing binaries.
2. The incorporation of dynamical tidal effects, such as adding the PN model of f -mode dynamical tides FMTIDAL [16], as their neglect is known to introduce biases in the inferred EOS [116, 117].
3. Extension to higher-order multipoles beyond the (2,2)-mode. This is of particular importance for unequal-mass and precessing systems, where more power is radiated in subdominant harmonics, and could play an important role in constraining the geometry of the merger and breaking the distance-inclination degeneracy.
4. Modelling tidal corrections to the amplitude, e.g. [29].

There are also numerous other avenues for extending the model that are being pursued. For example, there are higher-order tidal moments such as the octopolar and hexadecapolar terms [25]. The neutron star excites a spectrum of fluid modes beyond just the f -modes that need to be modelled, e.g. see [65, 118–120]. Including the effects of orbital eccentricity could also be important [121, 122], though this may be of less astrophysical significance [123].

Finally, we note that although we did not include precession effects in the analysis presented here, it is straightforward to follow the framework outlined in [124] to construct an approximate precessing BNS model by augmenting the BBH baseline [28–30, 125]. A notable benefit is that precession can help break the mass-spin degeneracy, leading to tighter constraints on the component masses [126, 127].

ACKNOWLEDGEMENTS

We thank Rossella Gamba for help with the C implementation of the TEOBRESUMS waveform model and useful comments on the manuscript. N.W. is supported by STFC, the School of Physics and Astronomy at the University of Birmingham and the Birmingham Institute for Gravitational Wave Astronomy. G.P. is very grateful for support from a Royal Society University Research Fellowship URF\R1\221500 and RF\ERE\221015, and gratefully acknowledges support from an NVIDIA Academic Hardware Grant. G.P. and P.S. acknowledge

support from STFC grant ST/V005677/1. P.S. also acknowledges support from a Royal Society Research Grant RG\R1\241327. Computations were performed using the University of Birmingham’s BlueBEAR HPC service, which provides a High Performance Computing service to the University’s research community, the Bondi HPC cluster at the Birmingham Institute for Gravitational Wave Astronomy as well as on resources provided by Supercomputing Wales, funded by STFC grants ST/I006285/1 and ST/V001167/1 supporting the UK Involvement in the Operation of Advanced LIGO. The fits were performed using Wolfram’s *Mathematica* [128]. Figures were generated using *Mathematica* and *Matplotlib* [129]. The version of TEOBRESUMS used in this work corresponds to git commit 128a406 [130]. This research has made use of data or software obtained from the Gravitational Wave Open Science Center (gwosc.org), a service of the LIGO Scientific Collaboration, the Virgo Collaboration, and KAGRA. This material is based upon work supported by NSF’s LIGO Laboratory which is a major facility fully funded by the National Science Foundation, as well as the Science and Technology Facilities Council (STFC) of the United Kingdom, the Max-Planck-Society (MPS), and the State of Niedersachsen/Germany for support of the construction of Advanced LIGO and construction and operation of the GEO600 detector. Additional support for Advanced LIGO was provided by the Australian Research Council. Virgo is funded, through the European Gravitational Observatory (EGO), by the French Centre National de Recherche Scientifique (CNRS), the Italian Istituto Nazionale di Fisica Nucleare (INFN) and the Dutch Nikhef, with contributions by institutions from Belgium, Germany, Greece, Hungary, Ireland, Japan, Monaco, Poland, Portugal, Spain. KAGRA is supported by Ministry of Education, Culture, Sports, Science and Technology (MEXT), Japan Society for the Promotion of Science (JSPS) in Japan; National Research Foundation (NRF) and Ministry of Science and ICT (MSIT) in Korea; Academia Sinica (AS) and National Science and Technology Council (NSTC) in Taiwan. This manuscript has the LIGO document number P2400286.

Appendix A: Parameter Space Fits

The full phenomenological fits of the five collocation points $\lambda^{(i)}$ needed to evaluate PHENOMGSF are given below. The phenomenological coefficients are listed in Tab. IV.

$$\lambda^{(1)}(\eta, \tilde{\Lambda}, \delta\tilde{\Lambda}) = \frac{1}{1 + a_1^{(1)}\tilde{\Lambda} + a_2^{(1)}\tilde{\Lambda}^2 + a_3^{(1)}\tilde{\Lambda}^3 + a_4^{(1)}\tilde{\Lambda}^4} \left[b_1^{(1)}(1 + d_{11}^{(1)}\delta\tilde{\Lambda} + d_{12}^{(1)}\delta\Lambda^2)\eta\tilde{\Lambda} - b_2^{(1)}(c_{11}^{(1)}(1 + d_{21}^{(1)}\delta\tilde{\Lambda} - d_{22}^{(1)}\delta\tilde{\Lambda}^2) - c_{12}^{(1)}(1 - d_{31}^{(1)}\delta\tilde{\Lambda} + d_{32}^{(1)}\delta\tilde{\Lambda}^2)\eta)\tilde{\Lambda}^4 + b_3^{(1)}(c_{21}^{(1)}(1 + d_{41}^{(1)}\delta\tilde{\Lambda} + d_{42}^{(1)}\delta\tilde{\Lambda}^2) + c_{22}^{(1)}(1 + d_{51}^{(1)}\delta\tilde{\Lambda} + d_{52}^{(1)}\delta\tilde{\Lambda}^2)\eta)\tilde{\Lambda}^5 \right] \quad (\text{A1})$$

$$\lambda^{(2)}(\eta, \tilde{\Lambda}, \delta\tilde{\Lambda}) = \frac{1}{1 + a_1^{(2)}\tilde{\Lambda} + a_2^{(2)}\tilde{\Lambda}^2 + a_3^{(2)}\tilde{\Lambda}^3} \left[b_1^{(2)}(c_{11}^{(2)}(1 + d_{11}^{(2)}\delta\tilde{\Lambda}) + c_{12}^{(2)}(1 + d_{21}^{(2)}\delta\tilde{\Lambda})\eta)\tilde{\Lambda} + b_2^{(2)}(c_{21}^{(2)}(1 + d_{31}^{(2)}\delta\tilde{\Lambda}) + c_{22}^{(2)}(1 + d_{41}^{(2)}\delta\tilde{\Lambda})\eta)\tilde{\Lambda}^2 + b_3^{(2)}(c_{31}^{(2)}(1 + d_{51}^{(2)}\delta\tilde{\Lambda}) + c_{32}^{(2)}(1 + d_{61}^{(2)}\delta\tilde{\Lambda})\eta)\tilde{\Lambda}^3 + b_4^{(2)}(1 + d_{71}^{(2)}\delta\tilde{\Lambda})\tilde{\Lambda}^4 \right] \quad (\text{A2})$$

$$\lambda^{(3)}(\eta, \tilde{\Lambda}, \delta\tilde{\Lambda}) = \frac{1}{1 + a_1^{(3)}\tilde{\Lambda} + a_2^{(3)}\tilde{\Lambda}^2 + a_3^{(3)}\tilde{\Lambda}^3} \left[b_1^{(3)}(c_{11}^{(3)}(1 + d_{11}^{(3)}\delta\tilde{\Lambda})\eta + c_{12}^{(3)}(1 + d_{21}^{(3)}\delta\tilde{\Lambda})\eta^2)\tilde{\Lambda} + b_2^{(3)}(c_{21}^{(3)}(1 + d_{31}^{(3)}\delta\tilde{\Lambda}) + c_{22}^{(3)}(1 + d_{41}^{(3)}\delta\tilde{\Lambda})\eta + c_{23}^{(3)}\eta^3)\tilde{\Lambda}^2 + b_3^{(3)}(c_{31}^{(3)} - c_{32}^{(3)}\eta)\tilde{\Lambda}^3 \right] \quad (\text{A3})$$

$$\lambda^{(4)}(\eta, \tilde{\Lambda}, \delta\tilde{\Lambda}) = \frac{1}{1 + a_1^{(4)}\tilde{\Lambda} + a_2^{(4)}\tilde{\Lambda}^2 + a_3^{(4)}\tilde{\Lambda}^3 + a_4^{(4)}\tilde{\Lambda}^4} \left[b_1^{(4)}(1 + d_{11}^{(4)}\delta\tilde{\Lambda})\eta^2\tilde{\Lambda} + b_2^{(4)}(c_{21}^{(4)}(1 + d_{21}^{(4)}\delta\tilde{\Lambda}) + c_{22}^{(4)}(1 + d_{31}^{(4)}\delta\tilde{\Lambda})\eta)\tilde{\Lambda}^2 + b_3^{(4)}(c_{31}^{(4)}(1 + d_{41}^{(4)}\delta\tilde{\Lambda}) + c_{32}^{(4)}(1 + d_{51}^{(4)}\delta\tilde{\Lambda})\eta + c_{33}^{(4)}\eta^2)\tilde{\Lambda}^3 + b_4^{(4)}\eta\tilde{\Lambda}^4 \right] \quad (\text{A4})$$

$$\lambda^{(5)}(\eta, \tilde{\Lambda}, \delta\tilde{\Lambda}) = \frac{1}{1 + a_1^{(5)}\tilde{\Lambda} + a_2^{(5)}\tilde{\Lambda}^2 + a_3^{(5)}\tilde{\Lambda}^3} \left[b_1^{(5)}\eta^2\tilde{\Lambda} + b_2^{(5)}(c_{11}^{(5)}(1 + d_{11}^{(5)}\delta\tilde{\Lambda}) + c_{12}^{(5)}(1 + d_{12}^{(5)}\delta\tilde{\Lambda})\eta)\tilde{\Lambda}^2 + b_3^{(5)}(c_{21}^{(5)} + c_{22}^{(5)}(1 + d_{21}^{(5)}\delta\tilde{\Lambda})\eta + c_{23}^{(5)}\eta^2)\tilde{\Lambda}^3 + b_4^{(5)}\eta^2\tilde{\Lambda}^4 + b_5^{(5)}\tilde{\Lambda}^5 \right] \quad (\text{A5})$$

Appendix B: GW170817 Posteriors

We present the full set of posteriors for the low-spin analysis of GW170817 in Fig. 14. Information on priors and recovered values can be found in Tab. III.

$x^{(1)}$ Value	$x^{(2)}$ Value	$x^{(3)}$ Value	$x^{(4)}$ Value	$x^{(5)}$ Value
$a_1^{(1)}$ 704.35868	$a_1^{(2)}$ 29.78722	$a_1^{(3)}$ 3.93783e13	$a_1^{(4)}$ 6.11502e13	$a_1^{(5)}$ 1.65802e12
$a_2^{(1)}$ 0.61592	$a_2^{(2)}$ 0.00029	$a_2^{(3)}$ 1.57134e10	$a_2^{(4)}$ 1.59883e11	$a_2^{(5)}$ 1.03757e10
$a_3^{(1)}$ 0.00037	$a_3^{(2)}$ 4.42273e-6	$a_3^{(3)}$ 4.06194e5	$a_3^{(4)}$ 1.50039e7	$a_3^{(5)}$ 2.06815e6
$a_4^{(1)}$ 9.36183e-8	$b_1^{(2)}$ -0.20692	$b_1^{(3)}$ -3.07059e12	$a_4^{(4)}$ -407.21516	$b_1^{(5)}$ -7.50478e12
$b_1^{(1)}$ -0.06132	$b_2^{(2)}$ -0.00013	$b_2^{(3)}$ -1.37322	$b_1^{(4)}$ -2.01764e14	$b_2^{(5)}$ -5.45113e9
$b_2^{(1)}$ -3.15315e-10	$b_3^{(2)}$ -6.05658e-7	$b_3^{(3)}$ -1.68496e7	$b_2^{(4)}$ -1.09596e11	$b_3^{(5)}$ -5.61410e7
$b_3^{(1)}$ 5.46894e-14	$b_4^{(2)}$ 7.15217e-11	$c_{11}^{(3)}$ -3.94830	$b_3^{(4)}$ -6.39775e8	$b_4^{(5)}$ 7.04369e4
$c_{11}^{(1)}$ 4.10522	$c_{11}^{(2)}$ -1.78228	$c_{12}^{(3)}$ 31.60021	$b_4^{(4)}$ 2.10833e5	$b_5^{(5)}$ 0.36838
$c_{12}^{(1)}$ -12.80678	$c_{12}^{(2)}$ 11.01742	$c_{21}^{(3)}$ 10.06460	$c_{21}^{(4)}$ 3.93019	$c_{11}^{(5)}$ 2.96697
$c_{21}^{(1)}$ 4.38039	$c_{21}^{(2)}$ 16.30702	$c_{22}^{(3)}$ -63.87040	$c_{22}^{(4)}$ -11.63559	$c_{12}^{(5)}$ -7.84667
$c_{22}^{(1)}$ -13.84189	$c_{22}^{(2)}$ -61.74570	$c_{23}^{(3)}$ 110.41652	$c_{31}^{(4)}$ 7.32205	$c_{21}^{(5)}$ 7.56107
$d_{11}^{(1)}$ -0.01033	$c_{31}^{(2)}$ 1.92755	$c_{31}^{(3)}$ 3.08006	$c_{32}^{(4)}$ -42.95971	$c_{22}^{(5)}$ -43.79735
$d_{12}^{(1)}$ 6.81023e-6	$c_{32}^{(2)}$ -3.65176	$c_{32}^{(3)}$ -8.31909	$c_{33}^{(4)}$ 70.66872	$c_{23}^{(5)}$ 70.23612
$d_{21}^{(1)}$ -0.00122	$d_{11}^{(2)}$ 0.02351	$d_{11}^{(3)}$ 0.04560	$d_{11}^{(4)}$ -0.02398	$d_{11}^{(5)}$ -0.03780
$d_{22}^{(1)}$ -8.60463e-7	$d_{21}^{(2)}$ 0.01609	$d_{21}^{(3)}$ 0.02267	$d_{21}^{(4)}$ -0.01840	$d_{12}^{(5)}$ -0.05580
$d_{31}^{(1)}$ -0.00154	$d_{31}^{(2)}$ -0.00046	$d_{31}^{(3)}$ -0.00144	$d_{31}^{(4)}$ -0.02534	$d_{21}^{(5)}$ 4.36021
$d_{32}^{(1)}$ -1.09916e-6	$d_{41}^{(2)}$ -0.00008	$d_{41}^{(3)}$ -0.00088	$d_{41}^{(4)}$ 0.00017	
$d_{41}^{(1)}$ -0.00072	$d_{51}^{(2)}$ -0.00024		$d_{51}^{(4)}$ 0.00013	
$d_{42}^{(1)}$ -5.84154e-7	$d_{61}^{(2)}$ -0.00095			
$d_{51}^{(1)}$ -0.00086	$d_{71}^{(2)}$ 0.00012			
$d_{52}^{(1)}$ -7.22994e-7				

TABLE IV. Values of the phenomenological coefficients of the parameter space fits, where x is a placeholder variable.

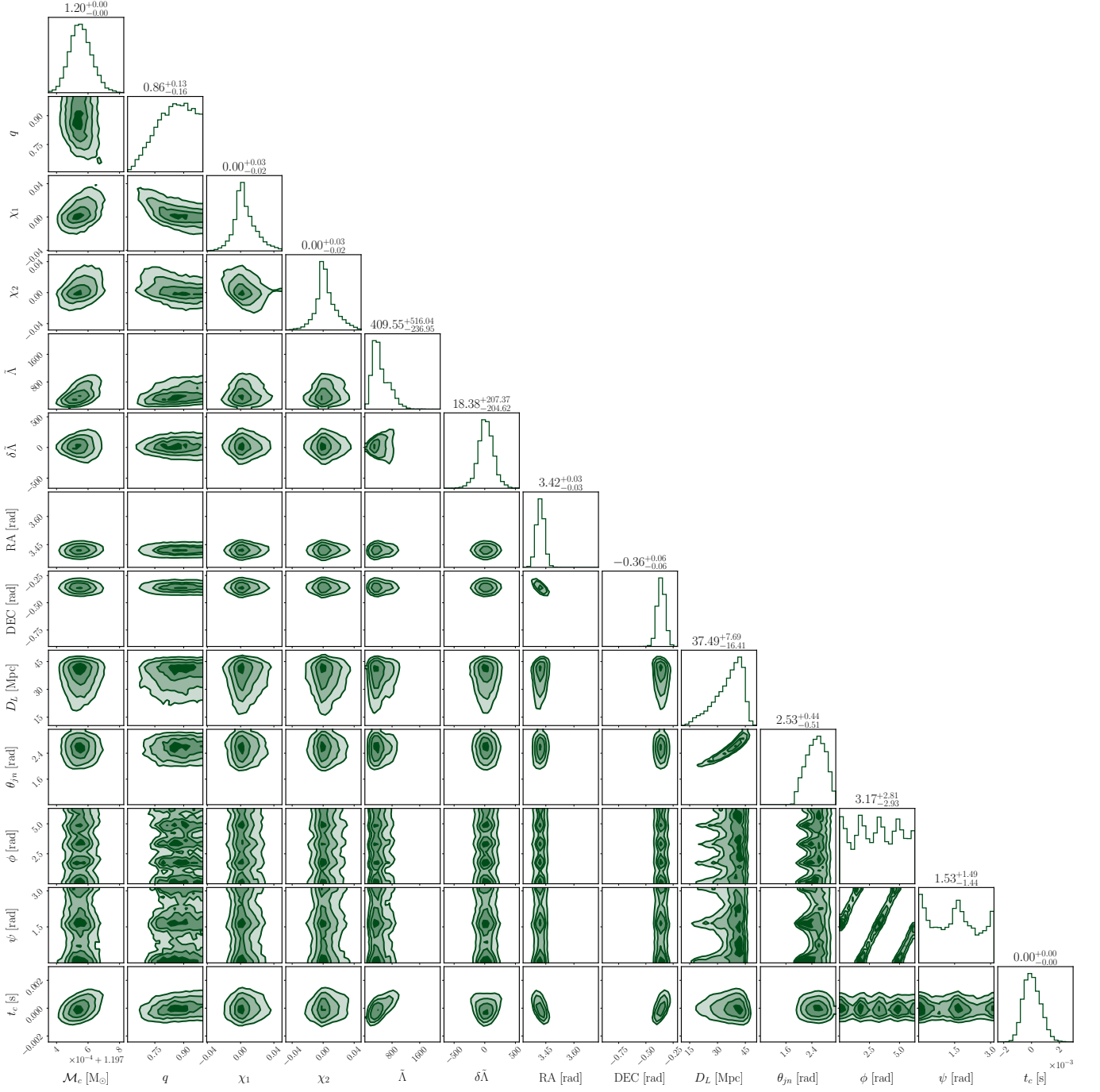


FIG. 14. 1D and 2D posteriors of all parameters obtained for GW170817 with IMRPHENOMXAS_PHENOMGSF. The geocentric time is shown with an offset of the true injected $t_c = 1187008882.4$ s for better visualisation.

-
- [1] E. E. Flanagan and T. Hinderer, Constraining neutron star tidal Love numbers with gravitational wave detectors, *Phys. Rev. D* **77**, 021502 (2008), [arXiv:0709.1915 \[astro-ph\]](#).
- [2] L. Wade, J. D. E. Creighton, E. Ochsner, B. D. Lackey, B. F. Farr, T. B. Littenberg, and V. Raymond, Systematic and statistical errors in a bayesian approach to the estimation of the neutron-star equation of state using advanced gravitational wave detectors, *Phys. Rev. D* **89**, 103012 (2014), [arXiv:1402.5156 \[gr-qc\]](#).
- [3] B. P. Abbott *et al.* (LIGO Scientific, Virgo), GW170817: Observation of Gravitational Waves from a Binary Neutron Star Inspiral, *Phys. Rev. Lett.* **119**, 161101 (2017), [arXiv:1710.05832 \[gr-qc\]](#).
- [4] B. P. Abbott *et al.* (LIGO Scientific, Virgo), Properties of the binary neutron star merger GW170817, *Phys. Rev. X* **9**, 011001 (2019), [arXiv:1805.11579 \[gr-qc\]](#).
- [5] G. Raaijmakers, S. K. Greif, K. Hebeler, T. Hinderer, S. Nisanke, A. Schwenk, T. E. Riley, A. L. Watts, J. M. Lattimer, and W. C. G. Ho, Constraints on the Dense Matter Equation of State and Neutron Star Properties from NICER’s Mass–Radius Estimate of PSR J0740+6620 and Multimessenger Observations, *Astrophys. J. Lett.* **918**, L29 (2021), [arXiv:2105.06981 \[astro-ph.HE\]](#).
- [6] M. C. Miller *et al.*, The Radius of PSR J0740+6620 from NICER and XMM-Newton Data, *Astrophys. J. Lett.* **918**, L28 (2021), [arXiv:2105.06979 \[astro-ph.HE\]](#).
- [7] D. Adhikari *et al.* (PREX), Accurate Determination of the Neutron Skin Thickness of ^{208}Pb through Parity-Violation in Electron Scattering, *Phys. Rev. Lett.* **126**, 172502 (2021), [arXiv:2102.10767 \[nucl-ex\]](#).
- [8] K. Chatziioannou, H. T. Cromartie, S. Gandolfi, I. Tews, D. Radice, A. W. Steiner, and A. L. Watts, Neutron stars and the dense matter equation of state: from microscopic theory to macroscopic observations, (2024), [arXiv:2407.11153 \[nucl-th\]](#).
- [9] B. T. Reed, F. J. Fattoyev, C. J. Horowitz, and J. Piekarewicz, Implications of PREX-2 on the Equation of State of Neutron-Rich Matter, *Phys. Rev. Lett.* **126**, 172503 (2021), [arXiv:2101.03193 \[nucl-th\]](#).
- [10] B. P. Abbott *et al.* (LIGO Scientific, Virgo), GW170817: Measurements of neutron star radii and equation of state, *Phys. Rev. Lett.* **121**, 161101 (2018), [arXiv:1805.11581 \[gr-qc\]](#).
- [11] J. Vines, E. E. Flanagan, and T. Hinderer, Post-1-Newtonian tidal effects in the gravitational waveform from binary inspirals, *Phys. Rev. D* **83**, 084051 (2011), [arXiv:1101.1673 \[gr-qc\]](#).
- [12] T. Damour, A. Nagar, and L. Villain, Measurability of the tidal polarizability of neutron stars in late-inspiral gravitational-wave signals, *Phys. Rev. D* **85**, 123007 (2012), [arXiv:1203.4352 \[gr-qc\]](#).
- [13] T. Abdelsalhin, L. Gualtieri, and P. Pani, Post-Newtonian spin-tidal couplings for compact binaries, *Phys. Rev. D* **98**, 104046 (2018), [arXiv:1805.01487 \[gr-qc\]](#).
- [14] B. Banihashemi and J. Vines, Gravitomagnetic tidal effects in gravitational waves from neutron star binaries, *Phys. Rev. D* **101**, 064003 (2020), [arXiv:1805.07266 \[gr-qc\]](#).
- [15] P. Landry, Rotational-tidal phasing of the binary neutron star waveform, (2018), [arXiv:1805.01882 \[gr-qc\]](#).
- [16] P. Schmidt and T. Hinderer, Frequency domain model of f -mode dynamic tides in gravitational waveforms from compact binary inspirals, *Phys. Rev. D* **100**, 021501 (2019), [arXiv:1905.00818 \[gr-qc\]](#).
- [17] Q. Henry, G. Faye, and L. Blanchet, Tidal effects in the equations of motion of compact binary systems to next-to-next-to-leading post-Newtonian order, *Phys. Rev. D* **101**, 064047 (2020), [arXiv:1912.01920 \[gr-qc\]](#).
- [18] Q. Henry, G. Faye, and L. Blanchet, Tidal effects in the gravitational-wave phase evolution of compact binary systems to next-to-next-to-leading post-Newtonian order, *Phys. Rev. D* **102**, 044033 (2020), [Erratum: *Phys.Rev.D* 108, 089901 (2023)], [arXiv:2005.13367 \[gr-qc\]](#).
- [19] T. Damour and A. Nagar, Effective One Body description of tidal effects in inspiralling compact binaries, *Phys. Rev. D* **81**, 084016 (2010), [arXiv:0911.5041 \[gr-qc\]](#).
- [20] D. Bini, T. Damour, and G. Faye, Effective action approach to higher-order relativistic tidal interactions in binary systems and their effective one body description, *Phys. Rev. D* **85**, 124034 (2012), [arXiv:1202.3565 \[gr-qc\]](#).
- [21] T. Hinderer *et al.*, Effects of neutron-star dynamic tides on gravitational waveforms within the effective-one-body approach, *Phys. Rev. Lett.* **116**, 181101 (2016), [arXiv:1602.00599 \[gr-qc\]](#).
- [22] J. Steinhoff, T. Hinderer, A. Buonanno, and A. Taracchini, Dynamical Tides in General Relativity: Effective Action and Effective-One-Body Hamiltonian, *Phys. Rev. D* **94**, 104028 (2016), [arXiv:1608.01907 \[gr-qc\]](#).
- [23] A. Bohé *et al.*, Improved effective-one-body model of spinning, nonprecessing binary black holes for the era of gravitational-wave astrophysics with advanced detectors, *Phys. Rev. D* **95**, 044028 (2017), [arXiv:1611.03703 \[gr-qc\]](#).
- [24] A. Nagar, S. Bernuzzi, W. Del Pozzo, G. Riemenschneider, S. Akcay, G. Carullo, P. Fleig, S. Babak, K. W. Tsang, M. Colleoni, F. Messina, G. Pratten, D. Radice, P. Rettengo, M. Agathos, E. Fauchon-Jones, M. Hannam, S. Husa, T. Dietrich, P. Cerdá-Duran, J. A. Font, F. Pannarale, P. Schmidt, and T. Damour, Time-domain effective-one-body gravitational waveforms for coalescing compact binaries with nonprecessing spins, tides, and self-spin effects, *Phys. Rev. D* **98**, 104052 (2018).
- [25] S. Akcay, S. Bernuzzi, F. Messina, A. Nagar, N. Ortiz, and P. Rettengo, Effective-one-body multipolar waveform for tidally interacting binary neutron stars up to merger, *Phys. Rev. D* **99**, 044051 (2019), [arXiv:1812.02744 \[gr-qc\]](#).
- [26] J. Steinhoff, T. Hinderer, T. Dietrich, and F. Foucart, Spin effects on neutron star fundamental-mode dynamical tides: Phenomenology and comparison to numerical simulations, *Phys. Rev. Res.* **3**, 033129 (2021), [arXiv:2103.06100 \[gr-qc\]](#).
- [27] R. Gamba *et al.*, Analytically improved and numerical-relativity informed effective-one-body model for coalescing binary neutron stars, (2023), [arXiv:2307.15125 \[gr-qc\]](#).

- qc].
- [28] T. Dietrich, S. Bernuzzi, and W. Tichy, Closed-form tidal approximants for binary neutron star gravitational waveforms constructed from high-resolution numerical relativity simulations, *Phys. Rev. D* **96**, 121501 (2017), [arXiv:1706.02969 \[gr-qc\]](#).
- [29] T. Dietrich, A. Samajdar, S. Khan, N. K. Johnson-McDaniel, R. Dudi, and W. Tichy, Improving the NR-Tidal model for binary neutron star systems, *Phys. Rev. D* **100**, 044003 (2019), [arXiv:1905.06011 \[gr-qc\]](#).
- [30] A. Abac, T. Dietrich, A. Buonanno, J. Steinhoff, and M. Ujevic, New and robust gravitational-waveform model for high-mass-ratio binary neutron star systems with dynamical tidal effects, *Phys. Rev. D* **109**, 024062 (2024), [arXiv:2311.07456 \[gr-qc\]](#).
- [31] S. Bernuzzi, A. Nagar, T. Dietrich, and T. Damour, Modeling the Dynamics of Tidally Interacting Binary Neutron Stars up to the Merger, *Phys. Rev. Lett.* **114**, 161103 (2015), [arXiv:1412.4553 \[gr-qc\]](#).
- [32] K. Kawaguchi, K. Kiuchi, K. Kyutoku, Y. Sekiguchi, M. Shibata, and K. Taniguchi, Frequency-domain gravitational waveform models for inspiraling binary neutron stars, *Phys. Rev. D* **97**, 044044 (2018), [arXiv:1802.06518 \[gr-qc\]](#).
- [33] P. Ajith *et al.*, Inspiral-merger-ringdown waveforms for black-hole binaries with non-precessing spins, *Phys. Rev. Lett.* **106**, 241101 (2011), [arXiv:0909.2867 \[gr-qc\]](#).
- [34] L. Santamaria *et al.*, Matching post-Newtonian and numerical relativity waveforms: systematic errors and a new phenomenological model for non-precessing black hole binaries, *Phys. Rev. D* **82**, 064016 (2010), [arXiv:1005.3306 \[gr-qc\]](#).
- [35] M. Hannam, P. Schmidt, A. Bohé, L. Haegel, S. Husa, F. Ohme, G. Pratten, and M. Pürrer, Simple Model of Complete Precessing Black-Hole-Binary Gravitational Waveforms, *Phys. Rev. Lett.* **113**, 151101 (2014), [arXiv:1308.3271 \[gr-qc\]](#).
- [36] G. Pratten, S. Husa, C. Garcia-Quiros, M. Colleoni, A. Ramos-Buades, H. Estelles, and R. Jaume, Setting the cornerstone for a family of models for gravitational waves from compact binaries: The dominant harmonic for nonprecessing quasicircular black holes, *Phys. Rev. D* **102**, 064001 (2020), [arXiv:2001.11412 \[gr-qc\]](#).
- [37] G. Pratten *et al.*, Computationally efficient models for the dominant and subdominant harmonic modes of precessing binary black holes, *Phys. Rev. D* **103**, 104056 (2021), [arXiv:2004.06503 \[gr-qc\]](#).
- [38] C. García-Quirós, M. Colleoni, S. Husa, H. Estellés, G. Pratten, A. Ramos-Buades, M. Mateu-Lucena, and R. Jaume, Multimode frequency-domain model for the gravitational wave signal from nonprecessing black-hole binaries, *Phys. Rev. D* **102**, 064002 (2020), [arXiv:2001.10914 \[gr-qc\]](#).
- [39] J. E. Thompson, E. Hamilton, L. London, S. Ghosh, P. Kolitsidou, C. Hoy, and M. Hannam, PhenomXO4a: a phenomenological gravitational-wave model for precessing black-hole binaries with higher multipoles and asymmetries, *Phys. Rev. D* **109**, 063012 (2024), [arXiv:2312.10025 \[gr-qc\]](#).
- [40] J. E. Thompson, E. Fauchon-Jones, S. Khan, E. Nitzoglía, F. Pannarale, T. Dietrich, and M. Hannam, Modeling the gravitational wave signature of neutron star black hole coalescences, *Phys. Rev. D* **101**, 124059 (2020), [arXiv:2002.08383 \[gr-qc\]](#).
- [41] A. Matas *et al.*, Aligned-spin neutron-star-black-hole waveform model based on the effective-one-body approach and numerical-relativity simulations, *Phys. Rev. D* **102**, 043023 (2020), [arXiv:2004.10001 \[gr-qc\]](#).
- [42] L. S. Finn and D. F. Chernoff, Observing binary inspiral in gravitational radiation: One interferometer, *Phys. Rev. D* **47**, 2198 (1993), [arXiv:gr-qc/9301003](#).
- [43] S. E. Field, C. R. Galley, J. S. Hesthaven, J. Kaye, and M. Tiglio, Fast prediction and evaluation of gravitational waveforms using surrogate models, *Phys. Rev. X* **4**, 031006 (2014), [arXiv:1308.3565 \[gr-qc\]](#).
- [44] N. J. Cornish, Fast Fisher Matrices and Lazy Likelihoods, (2010), [arXiv:1007.4820 \[gr-qc\]](#).
- [45] B. Zackay, L. Dai, and T. Venumadhav, Relative Binning and Fast Likelihood Evaluation for Gravitational Wave Parameter Estimation, (2018), [arXiv:1806.08792 \[astro-ph.IM\]](#).
- [46] D. Finstad and D. A. Brown, Fast Parameter Estimation of Binary Mergers for Multimessenger Follow-up, *Astrophys. J. Lett.* **905**, L9 (2020), [arXiv:2009.13759 \[astro-ph.IM\]](#).
- [47] N. J. Cornish, Heterodyned likelihood for rapid gravitational wave parameter inference, *Phys. Rev. D* **104**, 104054 (2021), [arXiv:2109.02728 \[gr-qc\]](#).
- [48] N. Leslie, L. Dai, and G. Pratten, Mode-by-mode relative binning: Fast likelihood estimation for gravitational waveforms with spin-orbit precession and multiple harmonics, *Phys. Rev. D* **104**, 123030 (2021), [arXiv:2109.09872 \[astro-ph.IM\]](#).
- [49] S. Vinciguerra, J. Veitch, and I. Mandel, Accelerating gravitational wave parameter estimation with multiband template interpolation, *Class. Quant. Grav.* **34**, 115006 (2017), [arXiv:1703.02062 \[gr-qc\]](#).
- [50] S. Morisaki, Accelerating parameter estimation of gravitational waves from compact binary coalescence using adaptive frequency resolutions, *Phys. Rev. D* **104**, 044062 (2021), [arXiv:2104.07813 \[gr-qc\]](#).
- [51] H. Antil, S. E. Field, F. Herrmann, R. H. Nochetto, and M. Tiglio, Two-step greedy algorithm for reduced order quadratures, *J. Sci. Comput.* **57**, 604 (2013), [arXiv:1210.0577 \[cs.NA\]](#).
- [52] P. Canizares, S. E. Field, J. R. Gair, and M. Tiglio, Gravitational wave parameter estimation with compressed likelihood evaluations, *Phys. Rev. D* **87**, 124005 (2013), [arXiv:1304.0462 \[gr-qc\]](#).
- [53] P. Canizares, S. E. Field, J. Gair, V. Raymond, R. Smith, and M. Tiglio, Accelerated gravitational-wave parameter estimation with reduced order modeling, *Phys. Rev. Lett.* **114**, 071104 (2015), [arXiv:1404.6284 \[gr-qc\]](#).
- [54] R. Smith, S. E. Field, K. Blackburn, C.-J. Haster, M. Pürrer, V. Raymond, and P. Schmidt, Fast and accurate inference on gravitational waves from precessing compact binaries, *Phys. Rev. D* **94**, 044031 (2016), [arXiv:1604.08253 \[gr-qc\]](#).
- [55] K. Yagi and N. Yunes, Approximate Universal Relations among Tidal Parameters for Neutron Star Binaries, *Class. Quant. Grav.* **34**, 015006 (2017), [arXiv:1608.06187 \[gr-qc\]](#).
- [56] C. A. Raithel and E. R. Most, Characterizing the Breakdown of Quasi-universality in Postmerger Gravitational Waves from Binary Neutron Star Mergers, *Astrophys. J. Lett.* **933**, L39 (2022), [arXiv:2201.03594 \[astro-ph.HE\]](#).

- [57] M. Favata, Systematic parameter errors in inspiraling neutron star binaries, *Phys. Rev. Lett.* **112**, 101101 (2014), [arXiv:1310.8288 \[gr-qc\]](#).
- [58] K. Hotokezaka, K. Kyutoku, Y.-i. Sekiguchi, and M. Shibata, Measurability of the tidal deformability by gravitational waves from coalescing binary neutron stars, *Phys. Rev. D* **93**, 064082 (2016), [arXiv:1603.01286 \[gr-qc\]](#).
- [59] T. Dietrich *et al.*, Matter imprints in waveform models for neutron star binaries: Tidal and self-spin effects, *Phys. Rev. D* **99**, 024029 (2019), [arXiv:1804.02235 \[gr-qc\]](#).
- [60] A. Nagar, F. Messina, P. Rettegno, D. Bini, T. Damour, A. Geralico, S. Akcay, and S. Bernuzzi, Nonlinear-in-spin effects in effective-one-body waveform models of spin-aligned, inspiralling, neutron star binaries, *Phys. Rev. D* **99**, 044007 (2019), [arXiv:1812.07923 \[gr-qc\]](#).
- [61] D. Bini and T. Damour, Gravitational self-force corrections to two-body tidal interactions and the effective one-body formalism, *Phys. Rev. D* **90**, 124037 (2014), [arXiv:1409.6933 \[gr-qc\]](#).
- [62] T. Damour and A. Nagar, Relativistic tidal properties of neutron stars, *Phys. Rev. D* **80**, 084035 (2009), [arXiv:0906.0096 \[gr-qc\]](#).
- [63] J. Provost, G. Berthomieu, and A. Rocca, Low Frequency Oscillations of a Slowly Rotating Star - Quasi Toroidal Modes, *A&A* **94**, 126 (1981).
- [64] W. C. G. Ho and D. Lai, Resonant tidal excitations of rotating neutron stars in coalescing binaries, *Mon. Not. Roy. Astron. Soc.* **308**, 153 (1999), [arXiv:astro-ph/9812116](#).
- [65] E. E. Flanagan and E. Racine, Gravitomagnetic resonant excitation of Rossby modes in coalescing neutron star binaries, *Phys. Rev. D* **75**, 044001 (2007), [arXiv:gr-qc/0601029](#).
- [66] R. Gamba, S. Bernuzzi, and A. Nagar, Fast, faithful, frequency-domain effective-one-body waveforms for compact binary coalescences, *Phys. Rev. D* **104**, 084058 (2021), [arXiv:2012.00027 \[gr-qc\]](#).
- [67] T. Dietrich, D. Radice, S. Bernuzzi, F. Zappa, A. Perego, B. Brügmann, S. V. Chaurasia, R. Dudi, W. Tichy, and M. Ujevic, CoRe database of binary neutron star merger waveforms, *Class. Quant. Grav.* **35**, 24LT01 (2018), [arXiv:1806.01625 \[gr-qc\]](#).
- [68] A. Gonzalez *et al.*, Second release of the CoRe database of binary neutron star merger waveforms, *Class. Quant. Grav.* **40**, 085011 (2023), [arXiv:2210.16366 \[gr-qc\]](#).
- [69] S. Bernuzzi *et al.*, *Core computational relativity* (2024).
- [70] T. Dietrich and T. Hinderer, Comprehensive comparison of numerical relativity and effective-one-body results to inform improvements in waveform models for binary neutron star systems, *Phys. Rev. D* **95**, 124006 (2017), [arXiv:1702.02053 \[gr-qc\]](#).
- [71] J. S. Read, B. D. Lackey, B. J. Owen, and J. L. Friedman, Constraints on a phenomenologically parameterized neutron-star equation of state, *Phys. Rev. D* **79**, 124032 (2009), [arXiv:0812.2163 \[astro-ph\]](#).
- [72] H. Nakano, A note on gravitational wave extraction from binary simulations, *Class. Quant. Grav.* **32**, 177002 (2015), [arXiv:1501.02890 \[gr-qc\]](#).
- [73] H. Nakano, J. Healy, C. O. Lousto, and Y. Zlochower, Perturbative extraction of gravitational waveforms generated with Numerical Relativity, *Phys. Rev. D* **91**, 104022 (2015), [arXiv:1503.00718 \[gr-qc\]](#).
- [74] R. L. Arnowitt, S. Deser, and C. W. Misner, The Dynamics of general relativity, *Gen. Rel. Grav.* **40**, 1997 (2008), [arXiv:gr-qc/0405109](#).
- [75] C. Reisswig and D. Pollney, Notes on the integration of numerical relativity waveforms, *Class. Quant. Grav.* **28**, 195015 (2011), [arXiv:1006.1632 \[gr-qc\]](#).
- [76] D. J. A. McKechnan, C. Robinson, and B. S. Sathyaprakash, A tapering window for time-domain templates and simulated signals in the detection of gravitational waves from coalescing compact binaries, *Class. Quant. Grav.* **27**, 084020 (2010), [arXiv:1003.2939 \[gr-qc\]](#).
- [77] I. Harry, S. Privitera, A. Bohé, and A. Buonanno, Searching for Gravitational Waves from Compact Binaries with Precessing Spins, *Phys. Rev. D* **94**, 024012 (2016), [arXiv:1603.02444 \[gr-qc\]](#).
- [78] T. Venumadhav, B. Zackay, J. Roulet, L. Dai, and M. Zaldarriaga, New search pipeline for compact binary mergers: Results for binary black holes in the first observing run of Advanced LIGO, *Phys. Rev. D* **100**, 023011 (2019), [arXiv:1902.10341 \[astro-ph.IM\]](#).
- [79] C. McIsaac, C. Hoy, and I. Harry, Search technique to observe precessing compact binary mergers in the advanced detector era, *Phys. Rev. D* **108**, 123016 (2023), [arXiv:2303.17364 \[gr-qc\]](#).
- [80] S. Schmidt, B. Gadre, and S. Caudill, Gravitational-wave template banks for novel compact binaries, *Phys. Rev. D* **109**, 042005 (2024), [arXiv:2302.00436 \[gr-qc\]](#).
- [81] D. Wadekar, T. Venumadhav, A. K. Mehta, J. Roulet, S. Olsen, J. Mushkin, B. Zackay, and M. Zaldarriaga, A new approach to template banks of gravitational waves with higher harmonics: reducing matched-filtering cost by over an order of magnitude, (2023), [arXiv:2310.15233 \[gr-qc\]](#).
- [82] D. Wadekar, T. Venumadhav, J. Roulet, A. K. Mehta, B. Zackay, J. Mushkin, and M. Zaldarriaga, A new search pipeline for gravitational waves with higher-order modes using mode-by-mode filtering, (2024), [arXiv:2405.17400 \[gr-qc\]](#).
- [83] B. P. Abbott *et al.* (LIGO Scientific, Virgo), Properties of the Binary Black Hole Merger GW150914, *Phys. Rev. Lett.* **116**, 241102 (2016), [arXiv:1602.03840 \[gr-qc\]](#).
- [84] B. P. Abbott *et al.* (LIGO Scientific, Virgo), GW170817: Observation of Gravitational Waves from a Binary Neutron Star Inspiral, *Phys. Rev. Lett.* **119**, 161101 (2017), [arXiv:1710.05832 \[gr-qc\]](#).
- [85] B. P. Abbott *et al.* (LIGO Scientific, Virgo), GWTC-1: A Gravitational-Wave Transient Catalog of Compact Binary Mergers Observed by LIGO and Virgo during the First and Second Observing Runs, *Phys. Rev. X* **9**, 031040 (2019), [arXiv:1811.12907 \[astro-ph.HE\]](#).
- [86] R. Abbott *et al.* (LIGO Scientific, Virgo), GWTC-2: Compact Binary Coalescences Observed by LIGO and Virgo During the First Half of the Third Observing Run, *Phys. Rev. X* **11**, 021053 (2021), [arXiv:2010.14527 \[gr-qc\]](#).
- [87] R. Abbott *et al.* (LIGO Scientific, KAGRA, VIRGO), Observation of Gravitational Waves from Two Neutron Star-Black Hole Coalescences, *Astrophys. J. Lett.* **915**, L5 (2021), [arXiv:2106.15163 \[astro-ph.HE\]](#).
- [88] R. Abbott *et al.* (KAGRA, VIRGO, LIGO Scientific), GWTC-3: Compact Binary Coalescences Observed by LIGO and Virgo during the Second Part of the Third Observing Run, *Phys. Rev. X* **13**, 041039 (2023),

- arXiv:2111.03606 [gr-qc].
- [89] R. Abbott *et al.* (LIGO Scientific, Virgo), GW190814: Gravitational Waves from the Coalescence of a 23 Solar Mass Black Hole with a 2.6 Solar Mass Compact Object, *Astrophys. J. Lett.* **896**, L44 (2020), arXiv:2006.12611 [astro-ph.HE].
- [90] R. Abbott *et al.* (LIGO Scientific, Virgo), Properties and Astrophysical Implications of the 150 M_{\odot} Binary Black Hole Merger GW190521, *Astrophys. J. Lett.* **900**, L13 (2020), arXiv:2009.01190 [astro-ph.HE].
- [91] A. G. Abac *et al.* (LIGO Scientific, VIRGO, KAGRA), Observation of Gravitational Waves from the Coalescence of a 2.5 – 4.5 M_{\odot} Compact Object and a Neutron Star, (2024), arXiv:2404.04248 [astro-ph.HE].
- [92] M. Cabero, A. B. Nielsen, A. P. Lundgren, and C. D. Capano, Minimum energy and the end of the inspiral in the post-Newtonian approximation, *Phys. Rev. D* **95**, 064016 (2017), arXiv:1602.03134 [gr-qc].
- [93] X. Jiménez-Forteza, D. Keitel, S. Husa, M. Hannam, S. Khan, and M. Pürrer, Hierarchical data-driven approach to fitting numerical relativity data for non-precessing binary black holes with an application to final spin and radiated energy, *Phys. Rev. D* **95**, 064024 (2017), arXiv:1611.00332 [gr-qc].
- [94] L. N. Trefethen, *Approximation theory and approximation practice, extended edition* (SIAM, 2019).
- [95] S. Marsat, Cubic order spin effects in the dynamics and gravitational wave energy flux of compact object binaries, *Class. Quant. Grav.* **32**, 085008 (2015), arXiv:1411.4118 [gr-qc].
- [96] A. Bohé, G. Faye, S. Marsat, and E. K. Porter, Quadratic-in-spin effects in the orbital dynamics and gravitational-wave energy flux of compact binaries at the 3PN order, *Class. Quant. Grav.* **32**, 195010 (2015), arXiv:1501.01529 [gr-qc].
- [97] E. Poisson, Gravitational waves from inspiraling compact binaries: The Quadrupole moment term, *Phys. Rev. D* **57**, 5287 (1998), arXiv:gr-qc/9709032.
- [98] R. A. Porto, A. Ross, and I. Z. Rothstein, Spin induced multipole moments for the gravitational wave flux from binary inspirals to third Post-Newtonian order, *JCAP* **03**, 009, arXiv:1007.1312 [gr-qc].
- [99] M. Levi and J. Steinhoff, Equivalence of ADM Hamiltonian and Effective Field Theory approaches at next-to-next-to-leading order spin1-spin2 coupling of binary inspirals, *JCAP* **12**, 003, arXiv:1408.5762 [gr-qc].
- [100] K. Yagi and N. Yunes, Approximate Universal Relations for Neutron Stars and Quark Stars, *Phys. Rept.* **681**, 1 (2017), arXiv:1608.02582 [gr-qc].
- [101] R. Abbott *et al.* (LIGO Scientific, Virgo), Open data from the first and second observing runs of Advanced LIGO and Advanced Virgo, *SoftwareX* **13**, 100658 (2021), arXiv:1912.11716 [gr-qc].
- [102] G. Ashton *et al.*, BILBY: A user-friendly Bayesian inference library for gravitational-wave astronomy, *Astrophys. J. Suppl.* **241**, 27 (2019), arXiv:1811.02042 [astro-ph.IM].
- [103] J. S. Speagle, dynesty: a dynamic nested sampling package for estimating Bayesian posteriors and evidences, *Mon. Not. R. Astron. Soc.* **493**, 3132 (2020), arXiv:1904.02180 [astro-ph.IM].
- [104] J. Aasi *et al.* (LIGO Scientific), Advanced LIGO, *Class. Quant. Grav.* **32**, 074001 (2015), arXiv:1411.4547 [gr-qc].
- [105] F. Acernese *et al.* (VIRGO), Advanced Virgo: a second-generation interferometric gravitational wave detector, *Class. Quant. Grav.* **32**, 024001 (2015), arXiv:1408.3978 [gr-qc].
- [106] Noise curves used for Simulations in the update of the Observing Scenarios Paper, <https://dcc.ligo.org/LIGO-T2000012/public> (2022).
- [107] A. Akmal, V. R. Pandharipande, and D. G. Ravenhall, The Equation of state of nucleon matter and neutron star structure, *Phys. Rev. C* **58**, 1804 (1998), arXiv:nucl-th/9804027 [nucl-th].
- [108] B. P. Abbott *et al.* (LIGO Scientific, Virgo), Model comparison from LIGO–Virgo data on GW170817’s binary components and consequences for the merger remnant, *Class. Quant. Grav.* **37**, 045006 (2020), arXiv:1908.01012 [gr-qc].
- [109] C. Cutler and E. E. Flanagan, Gravitational waves from merging compact binaries: How accurately can one extract the binary’s parameters from the inspiral wave form?, *Phys. Rev. D* **49**, 2658 (1994), arXiv:gr-qc/9402014.
- [110] E. Poisson and C. M. Will, Gravitational waves from inspiraling compact binaries: Parameter estimation using second postNewtonian wave forms, *Phys. Rev. D* **52**, 848 (1995), arXiv:gr-qc/9502040.
- [111] P. Schmidt, I. W. Harry, and H. P. Pfeiffer, Numerical Relativity Injection Infrastructure, (2017), arXiv:1703.01076 [gr-qc].
- [112] LIGO Scientific Collaboration, Virgo Collaboration, and KAGRA Collaboration, *LVK Algorithm Library - LALSuite*, Free software (GPL) (2018).
- [113] B. P. Abbott *et al.* (LIGO Scientific Collaboration and Virgo Collaboration), GWTC-1: A Gravitational-Wave Transient Catalog of Compact Binary Mergers Observed by LIGO and Virgo during the First and Second Observing Runs, *Phys. Rev. X* **9**, 031040 (2019), arXiv:1811.12907 [astro-ph.HE].
- [114] LIGO Scientific Collaboration, Virgo Collaboration, Gravitational Wave Open Science Center, <https://www.gw-openscience.org> (2019).
- [115] R. Gamba, M. Breschi, S. Bernuzzi, M. Agathos, and A. Nagar, Waveform systematics in the gravitational-wave inference of tidal parameters and equation of state from binary neutron star signals, *Phys. Rev. D* **103**, 124015 (2021), arXiv:2009.08467 [gr-qc].
- [116] G. Pratten, P. Schmidt, and T. Hinderer, Gravitational-Wave Asteroseismology with Fundamental Modes from Compact Binary Inspirals, *Nature Commun.* **11**, 2553 (2020), arXiv:1905.00817 [gr-qc].
- [117] G. Pratten, P. Schmidt, and N. Williams, Impact of Dynamical Tides on the Reconstruction of the Neutron Star Equation of State, *Phys. Rev. Lett.* **129**, 081102 (2022), arXiv:2109.07566 [astro-ph.HE].
- [118] S. Ma, H. Yu, and Y. Chen, Detecting resonant tidal excitations of Rossby modes in coalescing neutron-star binaries with third-generation gravitational-wave detectors, *Phys. Rev. D* **103**, 063020 (2021), arXiv:2010.03066 [gr-qc].
- [119] E. Poisson, Gravitomagnetic tidal resonance in neutron-star binary inspirals, *Phys. Rev. D* **101**, 104028 (2020), arXiv:2003.10427 [gr-qc].
- [120] W. C. G. Ho and N. Andersson, New dynamical tide constraints from current and future gravitational wave detections of inspiralling neutron stars, *Phys. Rev. D*

- [108](#), [043003](#) (2023), [arXiv:2307.10721 \[astro-ph.HE\]](#).
- [121] C. Chirenti, R. Gold, and M. C. Miller, Gravitational waves from f-modes excited by the inspiral of highly eccentric neutron star binaries, *Astrophys. J.* **837**, 67 (2017), [arXiv:1612.07097 \[astro-ph.HE\]](#).
- [122] P. Dutta Roy and P. Saini, Impact of unmodeled eccentricity on the tidal deformability measurement and implications for gravitational wave physics inference, (2024), [arXiv:2403.02404 \[astro-ph.HE\]](#).
- [123] D. R. Lorimer, Binary and Millisecond Pulsars, *Living Rev. Rel.* **11**, 8 (2008), [arXiv:0811.0762 \[astro-ph\]](#).
- [124] P. Schmidt, F. Ohme, and M. Hannam, Towards models of gravitational waveforms from generic binaries II: Modelling precession effects with a single effective precession parameter, *Phys. Rev. D* **91**, 024043 (2015), [arXiv:1408.1810 \[gr-qc\]](#).
- [125] M. Colleoni, F. A. R. Vidal, N. K. Johnson-McDaniel, T. Dietrich, M. Haney, and G. Pratten, IMRPhenomXP_NRTidalv2: An improved frequency-domain precessing binary neutron star waveform model, (2023), [arXiv:2311.15978 \[gr-qc\]](#).
- [126] K. Chatziioannou, N. Cornish, A. Klein, and N. Yunes, Spin-Precession: Breaking the Black Hole–Neutron Star Degeneracy, *Astrophys. J. Lett.* **798**, L17 (2015), [arXiv:1402.3581 \[gr-qc\]](#).
- [127] G. Pratten, P. Schmidt, R. Buscicchio, and L. M. Thomas, Measuring precession in asymmetric compact binaries, *Phys. Rev. Res.* **2**, 043096 (2020), [arXiv:2006.16153 \[gr-qc\]](#).
- [128] W. R. Inc., *Mathematica, Version 14.0*, Champaign, IL, 2024.
- [129] J. D. Hunter, Matplotlib: A 2d graphics environment, *Computing In Science & Engineering* **9**, 90 (2007).
- [130] S. Bernuzzi, A. Nagar, *et al.*, *TEOBResumS Bitbucket Respository* (2024).